Journal of Materials Research and Technology xxx (xxxx) 1–16

Contents lists available at ScienceDirect

Journal of Materials Research and Technology

journal homepage: www.elsevier.com

Steady states in severe plastic deformations and microstructure at normal and high pressure

Valery I. Levitas [a, b, *]

[a] Department of Aerospace Engineering, Iowa State University, Ames, IA, 50011, USA
[b] Department of Mechanical Engineering, Iowa State University, Ames, IA, 50011, USA

ARTICLE INFO

Handling editor: SN Monteiro

Keywords:
Severe plastic deformations
Perfectly plastic
Isotropic
And strain-path-independent
Behavior
Steady microstructures
Metals
Ceramics
And minerals
Pressure dependence of the yield strength
Coupled experimental-computational techniques

ABSTRACT

The main fundamental problem in studying plasticity and microstructure evolution is that they depend on five components of the plastic strain tensor $\boldsymbol{\varepsilon}_p$, its entire path ε_p^{path}, and pressure p and its path p^{path}, which leaves little hope of finding some general laws, especially at severe plastic straining and high pressures. Here, we review the validity of the following hypothesis for quasi-static material behavior after some critical level of cold severe plastic strain and some straining paths: initially isotropic polycrystalline materials behave like perfectly plastic, isotropic, and strain-path-independent with the corresponding limit surface of perfect plasticity and reach steady values of the crystallite/grain size and dislocation density, which are strain- and strain-path-independent. However, there are multiple steady microstructural states and corresponding limit surfaces of perfect plasticity. The main challenge is to find for which classes of loading paths ε_p^{path} and p^{path} material behaves along the same limit surface of perfect plasticity and steady microstructural state and for which loading paths ε_p^{path} and p^{path} there is a jump to the different limit surface of perfect plasticity and steady microstructural state. Various experimental, computational, and coupled experimental-computational techniques are analyzed, and some controversies and challenges are summarized.

Notations

$\boldsymbol{r} = \{r_i\}$ and $\boldsymbol{r_0} = \{r_{0j}\}$ position vectors of material points in the deformed and the reference (undeformed) states, respectively
$\boldsymbol{F} = \{F_{ij}\}$ deformation gradient
$\boldsymbol{U_p} = \{U_{pij}\}$ symmetric plastic stretch tensor
$\boldsymbol{R} = \{R_{ij}\}$ orthogonal rotation tensor
$\boldsymbol{d}$ deformation rate
$\boldsymbol{v}$ material particles velocity
ε_p plastic strain tensor
ε_p^{path} plastic strain tensor path
ε_p^L plastic strain measure ε_p^L defined by differential equation $\dot{\varepsilon}_p^L = \boldsymbol{d}$;
q equivalent or accumulated plastic strain (Odquist parameter)
l_0 and l lengths of a sample in the undeformed and deformed states
h_0 and h initial and final thickness of a sample compressed within Bridgman or diamond anvils
$\boldsymbol{\sigma} = \{\sigma_{ij}\}$ true (Cauchy) stress tensor
p pressure
p^{path} pressure path
$\overline{p}$ pressure averaged over the sample thickness h
$\boldsymbol{s} = \{s_{ij}\}$ deviatoric true stress
σ_M von Mises equivalent stress
$f\left(\boldsymbol{\sigma}, \varepsilon_p, \varepsilon_p^{path}\right) = 0$ yield surface
$\varphi(\boldsymbol{\sigma}) = 0$ fixed isotropic limit surface of perfect plasticity
$J_i(\boldsymbol{\sigma})$ three invariants of the stress tensor ;
J_i^L three invariants of $\varepsilon_p^{L,path}$

This article is part of a special issue entitled: Constitutive Modeling published in Journal of Materials Research and Technology.
* Department of Aerospace Engineering, Iowa State University, Ames, IA, 50011, USA.
E-mail address: vlevitas@iastate.edu.

https://doi.org/10.1016/j.jmrt.2025.03.060
Received 19 September 2024; Received in revised form 7 February 2025; Accepted 7 March 2025

m	equivalent plastic strain necessary for transition to the perfectly plastic state
Monotonic straining	straining path without sharp changes in directions in the strain space
Non-monotonic straining	straining path with sharp changes in directions in the strain space, which may include elastic unloading and reloading in different directions
Quasi-monotonic straining	non-monotonic straining started from the surface $\varphi(\sigma) = 0$ followed by monotonic straining increment with Δq exceeding some critical value q^* sufficient to reach the same surface $\varphi(\sigma) = 0$;
σ_y and τ_y	yield strengths at compression and shear, respectively
σ_{y0} and σ_∞	initial (at zero plastic strain) and maximum yield strength at zero pressure
b	pressure hardening coefficient
H	Brinell or Vickers hardness
β	ratio of the yield strength in compression after tension to stress reached at tension
δe_0	Bauschinger strain, after which curves for compression after tension reach the curve for monotonous tension
ρ	dislocation density
d	grain size;
τ_f	contact shear friction stress
$\widetilde{P}$	force divided by the area of the sample compressed in Bridgman anvils or twisted at HPT
SPD	severe plastic deformations
HPT	high-pressure torsion
DAC	diamond anvil cell
RDAC	rotational diamond anvil cell
XRD	x-ray diffraction
FEM	finite element method

1. Introduction

Processes involving severe plastic deformations (SPD) under normal and high pressure are common in producing nanostructured materials [1–7], materials shaping and surface processing (machining, polishing, turning, scratching, etc.), various high-pressure experiments and technologies, material synthesis under high pressure and SPD, in functional materials experiencing extreme stresses under contact friction, collision, and penetration, and in geophysics [8,9]. While formal continuum large-strain plasticity theory at normal and high pressure is quite well developed [10–12], determination of the evolution of the yield surface under multiaxial complex SPD is still challenging. *The main basic challenge in studying plasticity (and microstructure evolution) is that they depend not only on the reached plastic strain tensor ε_p but also on its entire path ε_p^{path} (e.g., various combinations of non-proportional multiaxial compressions/tensions and shears), which leaves a little hope to find some general rules due to an infinite number of independent parameters.*

We will focus the review on the quasi-static material deformations at room temperature. The state of the art in the field in 1980 is presented in review [13]. It includes the main experimental methods in studying large plastic deformations and related challenges. Thus, homogeneous strain in the tensile test is limited by necking, then stress-strain curves should be corrected using solutions to the necking problem. Compression test is complicated by barreling due to contact friction. Friction can be reduced by applying a special solid lubricant (e.g., MoS_2) [13] and producing multiple concentric grooves filled with different lubricants (e.g., graphite, powdered glass, and a mixture of powdered glass and BN powder for high-temperature experiments [14] (Fig. 1a)), which allowed to reach uniform equivalent strain q up to 1. Re-machining of the sample allows one to reach $q = 3$ [13], but friction and re-machining produce heterogeneity in the strain state. A single cylindrical groove on each face of the cylindrical sample filled with three-layer solid-semisolid-mineral oil lubricant (Fig. 1b) allowed to reach larger uniform strain, at least up to 4.5–6 times reduction in thickness and corresponding $q = 1.5$–1.79 [10,11,15]. This led to reaching a perfectly plastic plateau for six different metals, including Cu, Al, steels, and cast iron (see Fig. 8 below). Torsion of the cylindrical specimen is one more example of large-strain experiments in which linear plastic shear distribution along the radius is assumed [13], and stress-strain curves should be extracted utilizing a solution to the torsion problem. Torsion of a thin wall tube sample assumes uniform stress and strain states, but maximum strain is limited by buckling. Tensile tests or hardness measurements after cumulative drawing or rolling or any other SPD process (e.g., high-pressure torsion (HPT) [1–4,13,16–18] or equal channel extrusion [19–22]) are broadly used to find stress-strain curves. The largest equivalent plastic strain is reached with HPT, e.g., $q > 8.5 \times 10^4$ in Ref. [23] after 2515 rotations. In addition to the stress-strain curves, the microstructure evolution under SPD is studied in detail [1–4,7].

The main focus here will be on reviewing the following contradictory results. Steady states after SPD in terms of torque, hardness, stresses, grain size, and dislocation density (as well as in texture and fraction of low- and high-angle grain boundaries) are well-known in literature, particularly after HPT [1–7,16–18,24–26]. At the same time, there are many cases where they were not observed. In particular, in old and recent reviews [13,27–30], asymptotic perfectly plastic behav-

Fig. 1. Samples for almost frictionless uniform compression in the initial and final state. (a) Samples with multiple concentric grooves filled with different lubricants, which allowed to reach uniform equivalent strain q up to 1. Reproduced with permission from Ref. [14]. (b) Samples with a single cylindrical groove on each face filled with three-layer solid-semisolid-mineral oil lubricant allowed to reach $q = 1.5$–1.79 [10,11,15].

ior at large strains was either not reached or observed for most materials and loading modes. At ultra-SPD [23,31,32], small strain hardening rate and grain refinement reappear after steady yield strength and grain size regions. We will analyze various existing results within the frameworks of the continuum theory of plasticity and microstructure evolution.

In particular, we review the validity of the following hypothesis formulated in Refs. [10,11] and its possible generalization: *after some critical level of SPD and monotonic and quasi-monotonic straining paths, initially isotropic polycrystalline materials behave like perfectly plastic, isotropic, and strain-path-independent, with the fixed limit isotropic surfaces of perfect plasticity, and reach steady values of the crystallite/grain size and dislocation density, which are strain- and strain-path-independent.* Also, there are multiple steady fixed limit isotropic surfaces of perfect plasticity and steady values of the crystallite/grain size and dislocation density, which can be reached by different classes of the straining processes, after which material deforms according to the reached limit isotropic surfaces of perfect plasticity with the same crystallite/grain size and dislocation density for the same classes of straining (yet unknown).

2. Some definitions

Typical types of material behavior for 1D loading in terms of equivalent stress σ_M (e.g., von Mises true (Cauchy) stress) and equivalent plastic strain q, e.g., Odquist parameter are presented in Fig. 2. The main focus here is on the perfectly plastic behavior, i.e., at constant true equivalent stress, for large plastic strains (Fig. 2d).

A general 3D loading process is described by deformation gradient $\boldsymbol{F}=\{F_{ij}\}$, which is defined as $\boldsymbol{F}=\{\partial r_i/\partial r_{0j}\}$, where $\boldsymbol{r}=\{r_i\}$ and $\boldsymbol{r_0}=\{r_{0j}\}$ are the position vectors of material points in the deformed and the reference (undeformed) states [10–12]. For SPD, elastic strains can be neglected for simplicity of the discussion, and $\boldsymbol{F}=\boldsymbol{R}\bullet\boldsymbol{U_p}$ can be decomposed into orthogonal rotation tensor $\boldsymbol{R}=\{R_{ij}\}$ and symmetric stretch tensor $\boldsymbol{U_p}=\{U_{pij}\}$; $F_{ij}=R_{ik}U_{pkj}$. Here $\bullet$ denotes the contraction of tensors, and summation over the repeated subscript k is assumed. To avoid discussion about the independence of the constitutive equations of the rigid-body rotation (frame-indifference), we will assume that rotations are excluded by considering deformation in the rotating system, in which $\boldsymbol{F}=\boldsymbol{U}_p$. Strain-free state corresponds to $\boldsymbol{U}_p=\boldsymbol{I}$, where $\boldsymbol{I}=\{\delta_{ij}\}$ is the unit tensor and δ_{ij} is the Kronecker delta function ($\delta_{ij}=1$ for $i=j$ and $\delta_{ij}=0$ for $i\neq j$). For uniaxial straining $\boldsymbol{U}_p=\{l/l_0\}$, where l_0 and l are the lengths of a sample in the undeformed and deformed states. Plastic strain measure $\varepsilon_p=\{\varepsilon_{pij}\}$ can be some growing function of $\boldsymbol{U}_p$ equal to zero for $\boldsymbol{U}_p=\boldsymbol{I}$, for example, $\boldsymbol{U}_p-\boldsymbol{I}$ (l/l_0-1 for 1D loading), Lagrangian strain $0.5\left(\boldsymbol{U}_p^2-\boldsymbol{I}\right)$ $\left(0.5\left(l^2/l_0^2-1\right)\right.$, and logarithmic strain $ln\,\boldsymbol{U}_p$ $\left(ln\left(l/l_0\right)\right)$. The deformation rate is defined as $\boldsymbol{d}=\left(\dot{\boldsymbol{F}}\bullet\boldsymbol{F}^{-1}\right)_s=(\partial v/\partial r)_s=\left\{\left(\partial v_i/\partial r_j\right)_s\right\}$, where superscripts -1 and subscript s denote the inverse operation and symmetrization of the tensors, and $\boldsymbol{v}$ is material particles velocity. We focus on plastically incompressible (i.e., non-porous) materials because (a) porous materials exhibit strain hardening during compaction and cannot be discussed in the context of perfect plasticity, and (b) under high pressure and SPD, even powder materials are getting compact after some loading. Independent of the specific chosen plastic strain measure, for plastically incompressible materials, it has 5 independent components only. The first invariant of the tensor $\boldsymbol{d}$, d_{ii}, is zero for plastically incompressible materials, which means that $\boldsymbol{d}$ is a deviatoric tensor. For straining with fixed principal axes, the same is true for $ln\,\boldsymbol{U}_p$. The only strain measure ε_p^L defined in Refs. [10,11] by differential equation $\dot{\varepsilon}_p^L=\boldsymbol{d}$ is deviatoric for the general loading for plastically incompressible materials, i.e., the first invariant $J_1\left(\varepsilon_p^L\right)=0$. Strain measure ε_p^L depends on the entire straining path tensor $\boldsymbol{U}_p^{path}=\left\{U_{pij}^{path}\right\}$ prior to the current state $\boldsymbol{U}_p$. That means that, e.g., compression followed by torsion and torsion followed compression to the same $\boldsymbol{U}_p$ result in different ε_p^L. That is why this strain measure is called in Refs. [10,11] the nonholonomic one.

The equivalent strain (Odquist parameter) q is defined by a differential equation $\dot{q}=\left(2/3d_{ij}d_{ij}\right)^{0.5}=\left(2/3\,\dot{\varepsilon}_{pij}^L\dot{\varepsilon}_{pij}^L\right)^{0.5}$, i.e., q also depends on the entire straining path tensor ε_p^{path}. The yield surface can be generally presented in the form $f\left(\boldsymbol{\sigma},\varepsilon_p,\varepsilon_p^{path}\right)=0$, where $\boldsymbol{\sigma}=\{\sigma_{ij}\}$ is the true (Cauchy) stress tensor. It is convenient to decompose $\boldsymbol{\sigma}=-p\boldsymbol{I}+\boldsymbol{s}$, where $\boldsymbol{s}$ is the deviatoric stress and p is the pressure. In the geometric interpretation of the yield surface in the 6D stress $\boldsymbol{\sigma}$ space, it is fixed for the perfectly plastic material, expands in the loading direction for the hardening material, and shrinks in the loading direction for the softening material (Fig. 3a–c). Von Mises equivalent stress is defined as $\sigma_M=\left(3/2s_{ij}s_{ij}\right)^{0.5}$.

For materials that became perfectly plastic after SPD, the yield surface became fixed in the stress space. There are two options: the fixed yield surface is independent or depends on the plastic strain path prior to the current strain, i.e., it is described by $f(\boldsymbol{\sigma})=0$ or $f\left(\boldsymbol{\sigma},\varepsilon_p^{path}\right)=0$, respectively. For the first case, $f(\boldsymbol{\sigma})=0$ is the isotropic function (surface) because for initially isotropic material anisotropy could be strain-induced only, and since plastic strain and its paths are not arguments of $f(\boldsymbol{\sigma})$, there are no any sources for the description of anisotropy. Thus, $f(\boldsymbol{\sigma})$ is a function of three invariants $J_i(\boldsymbol{\sigma})$ of the stress tensor. In the second case, $f\left(\boldsymbol{\sigma},\varepsilon_p^{path}\right)=0$ (Fig. 3d), ε_p^{path} can formally produce fixed strain-induced anisotropy, e.g., due to texture or back stresses. However, suppose the further straining vector is much different from the prior straining vector (e.g., compression in one direction followed by compression in the orthogonal direction). In that case, it is very difficult to imagine that texture and back stress will not change and the yield surface remains fixed. Thus, anisotropic material cannot be, in general, perfectly plastic due to changes in texture and back stresses during general straining. Consequently, if the material is perfectly plastic, the yield surface $f\left(\boldsymbol{\sigma},\varepsilon_p^{path}\right)=0$ is isotropic in the stress space, i.e., depends on three invariants of the stress tensor $J_i(\boldsymbol{\sigma})$ and two independent invariants $J_i\left(\varepsilon_p^{path}\right)$ of ε_p^{path}. If the strain path is characterized in terms of $\varepsilon_p^{L,path}$ prior to the current state ε_p^L, this yield surface can be pre-

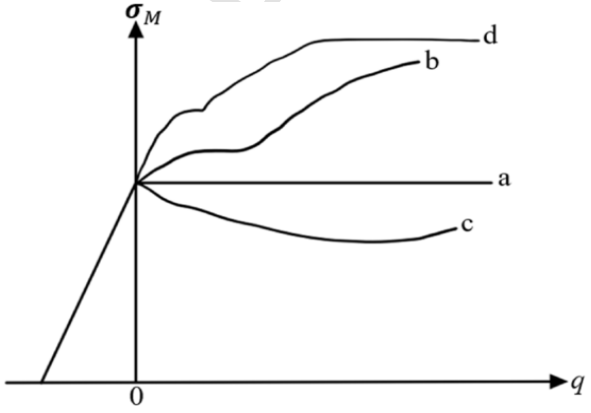

Fig. 2. Stress-plastic strain curves for typical material behaviors: perfectly plastic (a), hardening (b), softening (c) materials, and material that became perfectly plastic after SPD (d).

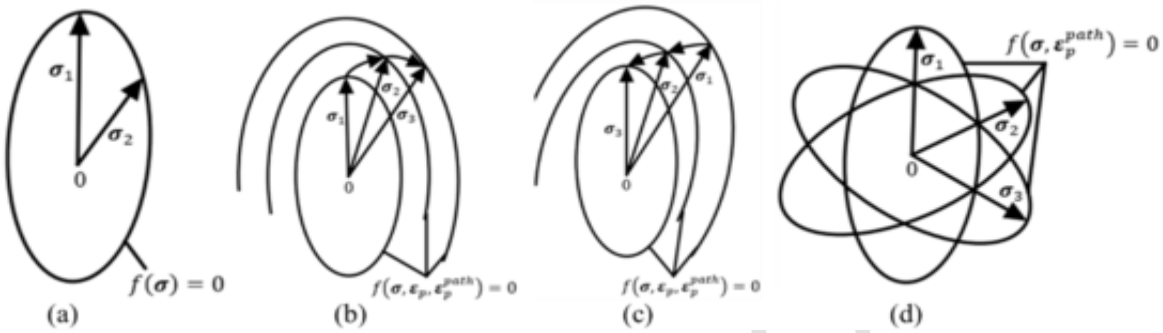

Fig. 3. Evolution of the yield surface for typical material behavior: perfectly plastic (a), hardening (b), and softening (c) materials, and materials that became perfectly plastic after SPD (d) but depends on the prior straining path. If material behavior is independent of the prior straining path, all three yield surfaces in (d) coincide.

sented as $f\left(J_i(\boldsymbol{\sigma}), J_2^L, J_3^L\right) = 0$, where J_i^L is the ith invariant of $\varepsilon_p^{L,path}$, since $J_1^L = 0$.

There is an apparent contradiction between the isotropic behavior of the perfectly plastic material after SPD and the known texture and back stresses (that depend on both ε_p and ε_p^{path}) of actual materials after SPD, which should be eliminated. It is suggested in Refs. [10,11] that in addition to the yield surface, there is a fixed isotropic limit surface of perfect plasticity $\varphi(\boldsymbol{\sigma}) = 0$. Then, above some level of SPD in monotonic straining (straining path without sharp changes in directions), the stress vector $\boldsymbol{\sigma}$ and the actual anisotropic yield surface $f\left(\boldsymbol{\sigma}, \varepsilon_p, \varepsilon_p^{path}\right) = 0$ reach a fixed isotropic limit surface of perfect plasticity $\varphi(\boldsymbol{\sigma}) = 0$ and both move along it. This means that the initially isotropic polycrystalline materials deform like perfectly plastic and isotropic with a strain path-independent limit surface of the perfect plasticity $\varphi(\boldsymbol{\sigma}) = 0$ (Fig. 4). We would like to reiterate that the isotropy of the surface $\varphi(\boldsymbol{\sigma}) = 0$ is the strict consequence of the initially isotropic material (i.e., anisotropy could be plastic strain-induced only) and independence of the of $\varphi(\boldsymbol{\sigma}) = 0$ of the ε_p and ε_p^{path}. Usually, as-received materials are anisotropic due to thermomechanical treatment which is not reported in detail. However, if this anisotropy is plastic-strain-induced, there is an initial isotropic state (obtained, e.g., by long enough annealing above the recrystallization temperature), which can be considered as an undeformed state, and condition for the initial isotropy is met.

For non-monotonic loading (i.e., for straining path with sharp changes in directions, which may include elastic unloading and reloading in different directions), materials behave according to their actual yield surface $f\left(\boldsymbol{\sigma}, \varepsilon_p, \varepsilon_p^{path}\right) = 0$, i.e., like anisotropic and dependent on plastic strain and its path (Fig. 4b and c). In Fig. 4c, non-monotonic straining (e.g., multiple rollings or passes of equal channel extrusion) leads to touching the limit surface of perfect plasticity $\varphi(\boldsymbol{\sigma}) = 0$. It is possible, in principle, to arrange such a non-monotonic straining, at which the end of the stress vector $\boldsymbol{\sigma}$ will not reach the surface $\varphi(\boldsymbol{\sigma}) = 0$, but this is not the case we want to focus on. In Fig. 4b, non-monotonic straining occurs after the surface $\varphi(\boldsymbol{\sigma}) = 0$ is reached. For this case, an additional hypothesis is that after some further straining, the stress vector and yield surface $f\left(\boldsymbol{\sigma}, \varepsilon_p, \varepsilon_p^{path}\right) = 0$ touch again the same limit surface of the perfect plasticity $\varphi(\boldsymbol{\sigma}) = 0$, and the material again behaves like perfectly plastic, isotropic, and strain path independent. That is

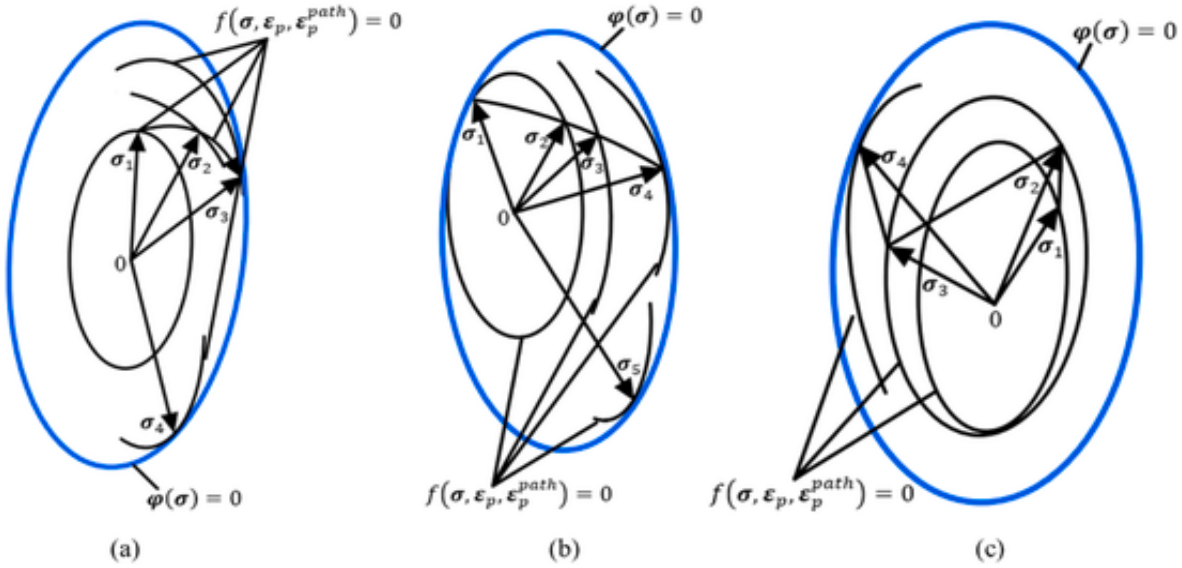

Fig. 4. Mutual location of the evolving yield surface $f\left(\boldsymbol{\sigma}, \varepsilon_p, \varepsilon_p^{path}\right) = 0$ and limit surface of perfect plasticity $\varphi(\boldsymbol{\sigma}) = 0$ for hardening material at monotonic (a) and non-monotonic straining after (b) and before (c) first reaching $\varphi(\boldsymbol{\sigma}) = 0$.

why for the case when the limit surface of the perfect plasticity $\varphi(\sigma)=0$ is already reached, we define quasi-monotonic straining, which is non-monotonic straining started from the surface $\varphi(\sigma)=0$ followed by monotonic straining increment with Δq exceeding some critical value q^*. For each material, after reaching the surface $\varphi(\sigma)=0$ and following non-monotonic straining, the critical value q^* is chosen so that the stress vector and yield surface $f\left(\sigma,\varepsilon_p,\varepsilon_p^{path}\right)=0$ touch again the same limit surface of the perfect plasticity $\varphi(\sigma)=0$ and material again behaves like perfectly plastic, isotropic, and strain path-independent. We will show in Sections 4 and 5 that $q^*\cong 0.1$, i.e., is surprisingly small.

Note that different σ_M-q curves for different loadings (torsion, compression, and tension) have been explained in Ref. [28] by different texture evolution and the Taylor factor (connecting averaged shear strain over all slip systems and deformation of a polycrystal) for these loading modes. If such a difference persists till a perfectly plastic plateau, it does not contradict the isotropy of the $\varphi(\sigma)=0$ surface because it can be described with the help of the first and third invariants of the stress tensor [12,33–35]. A comprehensive review of the texture evolution and its effect on plasticity is presented in Ref. [30].

3. Experimental confirmation of perfectly plastic behavior at monotonic straining under high pressure using compression with Bridgman anvils [10,11]

Here, we present the first experimental confirmation of perfectly plastic, isotropic, and strain path-independent material behavior under high pressure [10,11]. The following methods of testing were used in works [36–38]: a disc with the height h_0 is compressed between the Bridgman anvils [39] (which possess flat circular faces surrounded by conical surfaces to increase anvils' strength) down to the final height h while the applied force increases from zero to some constant value P for all experiments for each material. With small error, the working disc diameter d is a constant during deformation and equal to the anvil face diameter. After flowing outside the diameter d, brittle materials fracture, and ductile materials have small, low-stress contact with the inclined anvil surface. Therefore, the specific force $\widetilde{P}=4P/\pi d^2$ is also approximately the same at the end of all experiments. The goal of the experiments is to find the dependence $h(h_0)$ at $\widetilde{P}=const$ (Fig. 5), which qualitatively characterizes the resistance to shear. Stress state analyses in Ref. [36] utilized a simplified equilibrium equation and condition that the friction stress equals the yield strength in shear. This resulted in a large pressure gradient (qualitatively similar to that in Fig. 9). The fact that the material is in the plastic state means that an increase in applied force leads to a further reduction in the sample thickness. During compression, the straining is monotone, the plastic strains, particles rotation, and their paths are very heterogeneous within the sample due to contact friction and significantly vary with varying h_0. Examples of straining paths for different material points for a similar problem are determined in Ref. [40] with the finite element method (FEM). Particles rotations are essential because they change the orientation of the material anisotropy and lead to heterogeneous material, for which heterogeneity distribution depends on h_0. Also, different initial thicknesses lead to different material points remaining between anvil faces after reaching the prescribed load. All these should lead to different thicknesses h for different initial thicknesses h_0 unless the material behaves like perfectly plastic, isotropic, and independent of the straining path after some critical deformation.

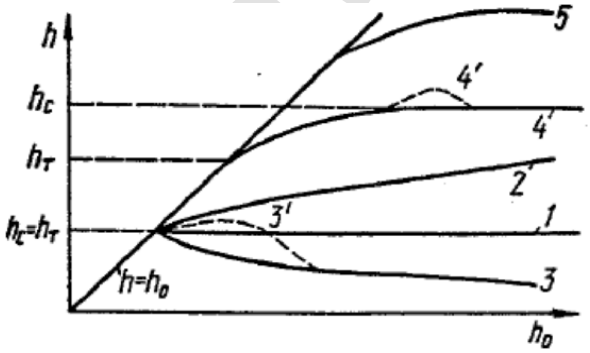

Fig. 5. Dependence of final height of the sample h on the initial height h_0 for constant final force for materials of various types [10,11]: 1 - perfectly plastic; 2 - hardening; 3 - softening: 3′-hardening material to a certain degree of straining, then - softening; 4 and 4' - material behaving like perfectly plastic, isotropic, and independent of the strain path after some critical deformation, 5 - material behaving like perfectly plastic after some critical deformation but dependent of the prior strain path.

Typical dependencies $h(h_0)$ for different types of materials obtained by a qualitative analysis based on known solutions to the compression problems by rough anvils are presented in Fig. 5. Below some critical initial thickness h_t, the material deforms elastically everywhere or in the major part of the sample, and $h=h_0$. For higher initial thicknesses, the sample deforms plastically, and the final thickness depends on h_0. Only for perfectly plastic isotropic material and material behaving like perfectly plastic, isotropic, and independent of the straining path after some critical deformation, there is a horizontal plateau in $h(h_0)$ curve.

In the experiments, for all the materials studied in Ref. [36] and (except four materials) in Refs. [37,38], a horizontal section on curve $h(ho)$ at $\widetilde{P}=const$ was found. That means that after some critical deformation, these materials behave like perfectly plastic, isotropic, and independent of the strain path. This is true for 43 from 47 materials studied in Refs. [36–38] related to various classes, like metals (indium, aluminum, lead, and copper), oxides (MnO_2, SnO_2, MoO_2, ZrO_2, and compacted powder of MgO with Bakelite varnish bond), various types of pyrophyllite (from Africa, Goto, Mitsuishi, Shokozon, natural blocked or compacted powder, also with different thermal treatments and addition of NaCl and Fe_2O_3), two types of graphite, $Al(OH)_3$, $Ca(OH)_2$, boron, BN, B_4C, H_3BO_3, NaCl, AgCl, KJ, KCl, KBr, pressboard, polystyrole, talc, marble, kobushnendo clay, micarex, Teflon, and two types of cardboard. One of the exceptions is a fabric cloth-based laminate [38], which is initially anisotropic material and should not exhibit perfectly plastic behavior. Three others are blocked and compacted with the Bakelite varnish bond powder of the $CaCO_3$ (limestone) and green silicon carbide [37,38], which exhibit a clear trend of curve $h(h_0)$ toward the horizontal line. These are probably not exceptions; just strain required for perfectly plastic behavior was not reached. Indeed, for blocked and compacted with the Bakelite varnish and polyvinyl alcohol limestones, such a transition to perfectly plastic behavior was found in experiments in Refs. [10,11]. It was found by the coincidence of the curves $\widetilde{P}(h)$ for different initial thicknesses h_0 starting with some degree of compression. This is a more general method than in Refs. [36–38] because it utilizes a broad range of applied forces and, consequently, achieved pressures, in contrast to a single selected force in Refs. [36–38].

The method used to prove the perfectly plastic behavior is sufficiently sensitive to detect possible deviations from the perfect plasticity since hardening and softening portions of the curves $h(h_0)$ are well visible for all materials before reaching a horizontal portion and a horizontal portion is lacking for the initially anisotropic fabric cloth-based laminate.

Values of the strain $m=ln\left(h_0/h\right)$ for transition to the perfectly plastic state for selected material are given in Table 1. This strain ranges from 0.368 for the compacted pyrophyllite powder to 1.262 for Armco-iron, which is the order of magnitude smaller than 10–20 reported in HPT works for metals [3,25,29].

Table 1
Values of the strain m for transition to the perfectly plastic state [10,11]. Reproduced with permission from Ref. [11].

Material	m
Blocked pyrophyllite	0.375
Pyrophyllite powder	0.368
Compacted powder of MnO with Bakelite varnish bond subjected to thermal treatment at 180 °C	0.421
Compacted pyrophyllite with NaCl (1:1) subjected to thermal treatment at 800 °C	0.873
Compacted powder of ZnO with Bakelite varnish bond subjected to thermal treatment at 180 °C	0.405
Compacted magnesite with Bakelite varnish bond subjected to thermal treatment at 180 °C	0.624
Cardboard	1.386
Copper M2	1.175
Armco-iron	1.262
Blocked lithographic limestone	0.405
Lithographic limestone compacted with Bakelite varnish bond	0.588
Lithographic limestone compacted with polyvinyl alcohol	0.629

4. Experimental confirmation of perfectly plastic behavior at quasi-monotonic straining: steady hardness [10,11]

Here, we discuss the first experimental confirmation of perfectly plastic, isotropic, and strain path-independent material behavior at quasi-monotonic straining based on achieving steady hardness [10,11]. Following [10,11], we will analyze below some of the published in Refs. [41,42] results of the experimental study of the hardness and microhardness (Vickers and Brinell hardness testers and PMT-3), of prestrained to SPD materials at room temperature. Prestraining was produced by deforming broaching and under tension and compression down to fracture of cylindrical specimens [41], as well as by various surface treatment techniques [42]. Deforming broaching consists of broaching through bushing a broach whose diameter d is larger than the bushing diameter by the value of interference to increase the bushing hole. The process is repeated multiple times with a gradual increase in the broach diameters. Work [41] describes 6 ductile steels 10, 20, 30ХГСА, 40ХНМА, 38ХМЮА, and У8, alloys Д16Т and АК6) and 3 low ductile metal В93, В95 and Мл5пч. Correspondence between marking in Russian literature and literature in the USA, UK, and some other countries can be found in Ref. [34]; the chemical composition for all non-US marked alloys is given in Table 4.

The contact friction conditions, bushing wall thickness, angle of the broach inclination, interference, and the number of runs (up to 40) have been varied in the experiments. While the average over the wall thickness strain did not exceed 0.2, the contact friction caused the local shear strains in the thin surface layer to be several hundred percent [10,11,43], determined in particular by grain deformation.

The measured hardness on the internal surface of the bushings in a thin contact layer increased with a number of broaching passes, reached the maximum value, and remained steady during further deformation. The critical point is that the steady hardness for each material is independent of the varied geometric and processing parameters and is the same while measured perpendicularly to the bushing surface and in the meridional section after cutting the bushing.

The strain paths during broaching are very complicated, occurring beyond contact zones ahead and behind the broach, but mainly in the contact region under large normal and shear contact stresses, which, depending on the process conditions, may vary by two orders of magnitude [41,43]. There is elastic unloading and reloading after each run in slightly different directions of the stress vector because of changed geometry and related contact conditions, conditions beyond the contact process zone, and heterogeneity of the residual stress-strain fields.

Consequently, the loading is non-monotone, but shear dominated, similar to that in the contact layer during the compression in Bridgman anvils and diamond anvil cells (DAC), in which metallic or ceramic anvils are substituted with the diamond anvils, but at lower pressures. Thus, the steady hardness for each material is independent of plastic strain and strain paths realized in the broaching with different controlling parameters.

In addition, tensile testing of cylindrical specimens made of 8 studied ductile metals and compressive testing of 3 metals with low ductility were performed till fracture [41]. After that, Vickers hardness was measured in the broken neck of the tensile specimens along the axis and in the fractured cross-section of the compressed specimens. Fig. 6 shows the relationship between maximum hardness in the surface layer of the bushing after deforming broaching and hardness in the neck of destroyed specimens or the cross-section of compressed till fracture specimens [41]. Fig. 6 demonstrates a good correlation between steady hardnesses after broaching and the hardness of the fracture surface for all 11 metals. Consequently, the same steady hardness is also achieved on the fracture surfaces of the ductile and brittle materials, which means that large enough local plastic strain is reached (much larger than the averaged strains) and that steady hardness is independent of the straining paths for the studied paths. This is a very unexpected and important result. The straining path for points of the fractured surfaces during the testing is complex but monotone. However, the straining path for the specimen fracturing followed by hardness measurement is non-monotone because of unloading followed by loading in a different direction of the stress vector. In hardness measurement, the loading is monotone, and the increment of Δq in the region adjoining the indenter and influencing hardness is in the range of 0.05–0.1 for the ball indentation and 0.02–0.3 for the cone indentation [44]. The known relationship between σ_y and hardness H, $\sigma_y = k\,H$, with a factor k in the range from 1/3 to 0.386 [13,45–48], allows to connect σ_y and H. Consequently, steady hardness obtained after different types of SPD here and in other SPD processes [1–7,24] also means steady yield strength under normal pressure, i.e., perfectly plastic behavior. While factor k may depend on strain (due to strain hardening) and strain mode [13,45–48], these effects are reduced by approaching the perfectly plastic stage.

Results in Ref. [41] that hardness at the fracture surfaces reaches the same value as steady hardness after multiple broaching is counterintuitive and of great importance. They should be checked and supplemented by microstructural measurements, which should shed light on the possible reasons and mechanisms.

An additional method to determine a steady hardness was suggested in Ref. [49]. When the apex of a conical sample is compressed along its axis, a facet forms on which $q > m$. This method is simpler than fractur-

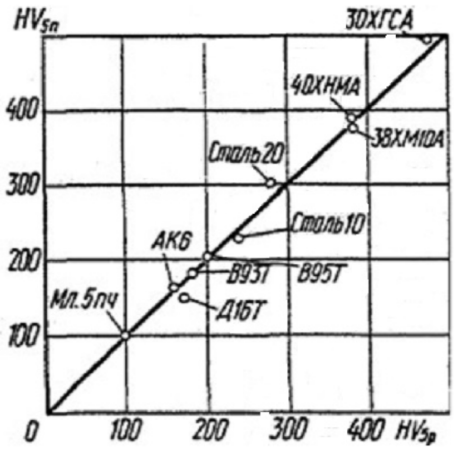

Fig. 6. Relationship between the steady hardness HV of the internal surface of the bushings after deforming broaching (subscript n) and hardness in the neck of the fractured specimen or broken cross-section of compressed to fracture (subscript p) specimen [41].

ing tensile or compressive samples and requires lower force. Still, it gives the same value as the steady hardness of the latter. This is one more example of the independence of the steady hardness of the plastic straining path.

SPD was also created by various methods of surface plastic hardening: grit blasting, centrifugal-ball treatment, spinning with rollers and balls, with variations of pressure, the diameter of balls, longitudinal feeding, and the number of runs [42]. It was found for eight grades of carbon steel with variations in the carbon contents from 0 to 1.2 % that the steady hardness was reached, independent of the hardening method and the treatment modes. The straining for surface hardening is strongly non-monotone, with multiple unloadings and reloadings, and the straining paths strongly depend on the hardening method and the treatment modes.

Thus, the above experimental results for deforming broaching, fracture, and surface treatment imply that the steady hardness is reached for each tested metal, independent of the monotone and non-monotone straining paths.

Let us consider the process of measuring the Vickers or Brinell hardness of a material after heterogeneous SPD. During SPD, material particles experience not only straining but also rigid-body translations and rotations. Therefore, if during heterogeneous SPD, the material was or became hardening (softening), anisotropic, and nonuniform, then the distributions of inhomogeneity, anisotropy, and yield surfaces evolve during the following straining. If one knows these distributions, then, solving the problem of hardness indentation, one can determine the hardness, i.e., the ratio of the force to the impression area. Simple analysis shows that only for initially perfectly plastic, isotropic, and homogeneous material or material that behaves like perfectly plastic, isotropic, and homogeneous after some critical straining, further straining does not change the uniform distribution of the fixed isotropic limit surface of the perfect plasticity $\varphi(\boldsymbol{\sigma})=0$. That is why hardness will be steady for further plastic straining. For all other types of materials, their hardness should evolve. Even if the material behaves like perfectly plastic, isotropic, and homogeneous after some critical straining, but its behavior depends on the straining path, the heterogeneous SPD process leads to the heterogeneous distribution of fixed isotropic yield surfaces $\varphi\left(J_i(\boldsymbol{\sigma}), J_2^L, J_3^L\right)=0$, which depends on the straining process · Then, hardness also depends on the straining process. Thus, *steady hardness after all the above deformation processes implies that material deforms like perfectly plastic and isotropic with a strain path-independent limit surface of the perfect plasticity* $\varphi(\boldsymbol{\sigma})=0$.

Since for Vickers hardness measuring, $0.02<\Delta q<0.3$ [44], the value q^* in the definition of the quasi-monotonic straining for all studied materials has the order of magnitude of these values. Note that the maximum deviation from the mean values of the limit hardness for all materials studied in Refs. [41,42] did not exceed ± 5 %, within the limits of errors for the hardness measuring. However, it means that if some parameters (plastic strain and its path, anisotropy, etc.) change the hardness by less than 5 %, it is impossible to strictly conclude it does not affect the limit surface of the perfect plasticity $\varphi(\boldsymbol{\sigma})=0$.

Note that the steady hardness independent of the straining path under compression between anvils was also proved for the compacted limestone [10,11]. Thus, it behaves like perfectly plastic, isotropic, and independent of the straining path not only under monotonic compression but also under quasi-monotonic loading.

5. Estimate of parameter q^* for quasi-monotonic loading

Based on limited data, the following procedure was suggested in Refs. [10,11] utilizing some finite-strain data on the Bauschinger effect obtained in Refs. [44,46].

(a) Stress-logarithmic strain curves for compression after tension for some metals coincide with a curve for monotonous tension (Fig. 7a) after exceeding some strain (Bauschinger strain δe_0) shown in Fig. 7c.
(b) Variation of the ratio β of the yield strength in compression after tension to stress reached at tension is getting steady and in the range of 0.4–0.6 after prestraining of 0.35 (Fig. 7b).
(c) Bauschinger strain saturates at the level of 0.06 after prestraining exceeding 0.2.

These results, extrapolated to SPD, led to the conclusion that if the limit surface of perfect plasticity $\varphi(\boldsymbol{\sigma})=0$ is reached, for the reverse loading (showing maximum deviation of the yield surface $f\left(\boldsymbol{\sigma}, \varepsilon_p, \varepsilon_p^{path}\right)=0$ from the limit surface $\varphi(\boldsymbol{\sigma})=0$), the same limit surface $\varphi(\boldsymbol{\sigma})=0$ will be reached on the opposite side after exceeding the Bauschinger strain. The Bauschinger strain is identified as a strain q^* for quasi-monotonic loading and is on the order of 0.06–0.1 and is considered the upper bound for other than the reversed loading. Such a definition is evident if the only source of the anisotropy is the back stress and less justified if shape change and rotation of the yield surface due to texture is considered. Still, $q^*\cong 0.1$ is consistent with reaching the same steady hardness after very different modes and strain paths during SPD, as discussed above. Quite a general 3D model for complex SPD with kinematic hardening was developed in Refs. [10,11] based on a generalization of experiments in Refs. [44,46].

6. Constitutive equations for large-strain homogeneous loading

As we mentioned, in numerous papers and reviews [13,27–30], asymptotic perfectly plastic behavior at large strains is either not reached or not observed for most materials and loading modes. That is why most textbook approximations of 1D stress-strain curves represent versions of power functions (e.g., Ludwick (1909), Holloman (1944), Swift (1947), and Ramberg and Osgood (1943)), for which stress tends to infinity for infinite strain [35]. The most popular model with finite steady stress for infinite strain was the Voce model [50,51].

$$\sigma=\sigma_{y0}+\left(\sigma_\infty-\sigma_{y0}\right)\left[1-exp\left(-n\varepsilon\right)\right], \tag{1}$$

where σ_{y0} and σ_∞ are initial and maximum yield strength asymptotically reached at infinity, ε is the logarithmic strain, and n is a material parameter. Eq. (1) has been used to describe stress-strain curves for 8 copper alloys for a 60 % reduction in height (i.e., $\varepsilon=0.916$), for which a steady state is not reached, but there is a tendency to it. In their review, Kocks and Mecking [28] did not observe a tendency to complete saturation of the strain hardening for the accumulated strain of 2. They mentioned that the Voce rule does not describe the whole stress-strain curve, but σ_∞ is the convenient scaling parameter to derive more general approximations for the stress-strain curves, which do not show perfectly plastic behavior.

Since these results were in contradiction with the existence of the limit surface of perfect plasticity formulated in Refs. [10,11] and in Sections 2-4, samples with groves filled with a special multilayer lubricant (Fig. 1b) were optimized and used to study uniform compression [10,11,15] of 7 metals (Fig. 8). For all of them, a perfectly plastic plateau is observed, and all curves are well described by equations

$$\sigma=\sigma_\infty-\left(\sigma_\infty-\sigma_{y0}\right)\left(\frac{q}{m}-1\right)^2 \quad for\ \frac{q}{m}\le 1; \tag{2}$$

$$\sigma=\sigma_\infty\ for\ \frac{q}{m}>1.$$

Eq. (2) is the simplest parabolic approximation utilizing conditions $\sigma(0)=\sigma_{y0}$, $\sigma(m)=\sigma_\infty$, and smooth transition to the plateau $d\sigma/dq=0$ for $q=m$. Material parameters in Eq. (2) are presented in Table 2. For 3 of 4 steels and copper, $m\ge 1$; it is quite small, 0.44, for the cast iron.

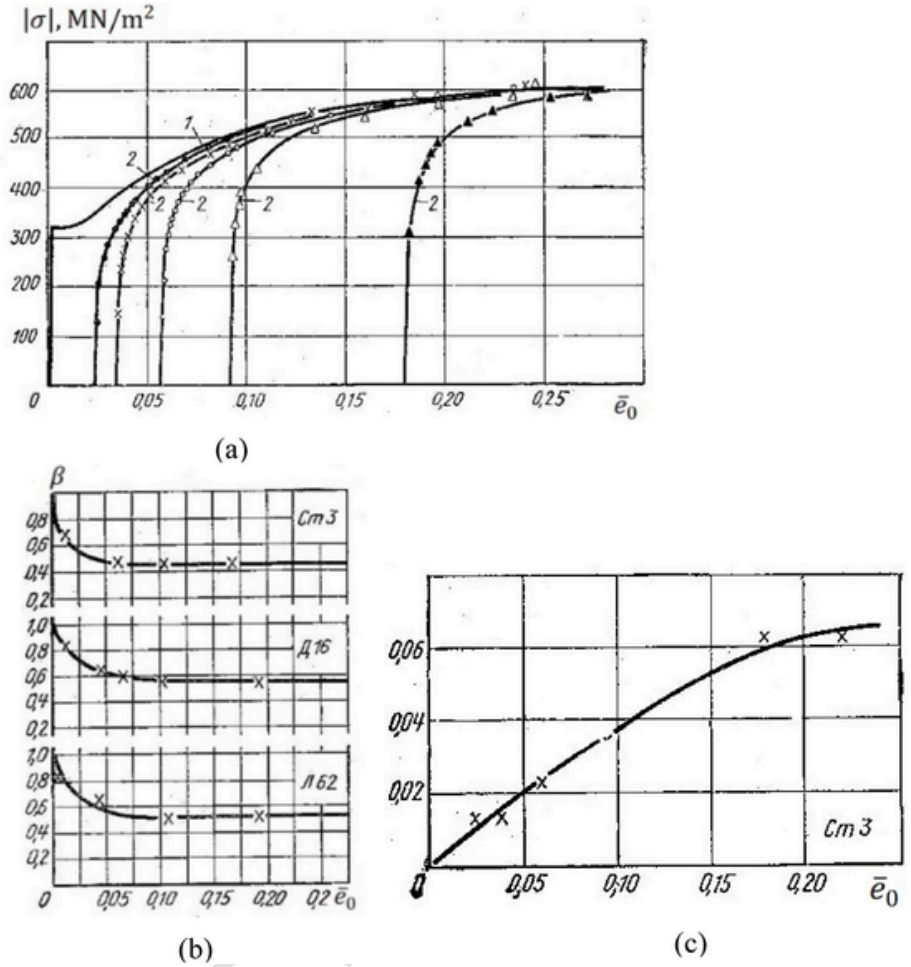

Fig. 7. (a) Stress $|\sigma|$ -logarithmic strain $\bar{e}_0$ curves for compression (1) after tension (2) for steel Cm 3 (St 3). (b) Variation of the ratio β of the yield strength in compression after tension to stress reached at tension at logarithmic strain $\bar{e}_0$ for steel Cm 3 (St 3), aluminum alloy $Д16$ $(D16)$, and brass $Л62$ (L62). (c) Bauschinger strain δe_0, after which curves for compression after tension reach the curve for monotonous tension versus logarithmic strain $\bar{e}_0$ at tension. Reproduced from Ref. [46].

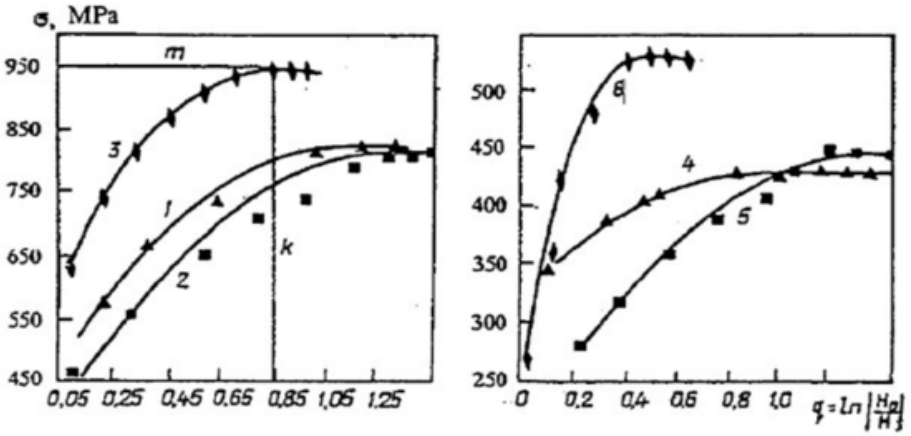

Fig. 8. Stress-strain curves for uniform compression using samples in Fig. 1b for steels 12 KhN3A (1), 45 (2), and U8A (3), copper M2 (4), steel St 3 (5), and cast iron VCh-50 (6). Symbols are for experimental points, and curves are described by Eq. (2). Reproduced with permission from Ref. [15].

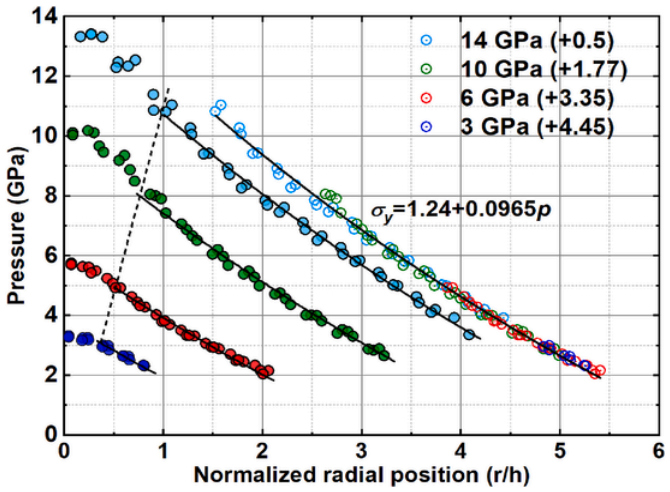

Fig. 9. Experimental radial pressure distributions in ω-Zr (symbols) compressed in DAC to four different loads, designated by a maximum pressure at the sample center, are well described by Eq. (4) with $\sigma_\infty = 1.24$ GPa and $b = 0.0965$ (solid lines). The dashed line separates the data not used for the determination of the yield strength because Eq. (4) is not applicable near the sample center due to the reduction in friction stress to zero at the symmetry axis. The upper unified curve combines all data by translating each curve (which is allowed by Eq. (3)) along the horizontal axis by the distance shown in parentheses. Reproduced with permission from Ref. [59].

Table 2
Material parameters in Eq. (2). Reproduced with permission from Ref. [15].

Material	m	σ_∞, MPa	σ_{y0}, MPa
Copper M2 annealed	1.0 1.57	430	330
		430	183.5
Steels			
St 3	1.35	445	200
45	1.3	815	370
12KhN3A	1.1	820	430
U8A	0.82	942.5	555
Cast Iron VCh-50	0.44	527.5	250

It should be mentioned that while the value σ_∞ for Cu corresponds to steady hardness from other studies, σ_{y0} is too large. This implies that Cu in Ref. [15] was not in the annealed state but rather plastically predeformed. If one utilizes the value $\sigma_{y0} = 183.5\ MPa$ for annealed Cu from various sources, then the same experimental data are described with $m = 1.57$ (Table 2), which was used in Ref. [52] for FEM simulations of HPT of Cu.

Note that Eq. (1) gives a much worse description of experiments in Ref. [15] than Eq. (2): It either describes well initial portion of the curves and then is much below than experimental points for larger strains and gives much larger m or describes well experimental points at $q=m$ but then is much higher than experimental points for intermediate strains.

It is clear that for elevated temperature, the transition to perfect plastic behavior occurs at smaller m, making detection easier. This was shown in Ref. [14] for 1100 Al and Fe–2 %S alloy for several temperatures and strain rates. By definition, above the recrystallization temperature, $m = 0$. This condition was utilized in Refs. [10,11] to approximately include temperature in Eq. (2).

7. Steady torque during HPT and steady hardness and microstructure after SPD

Starting with pioneering Bridgman's experiments [39] and followed by modern works on HPT [1–4,16–18], the initial increase of the torque with a number of rotations of an anvil at constant axial force saturates and leads to a constant (steady) value. This was interpreted as a transition to the perfectly plastic behavior, which explicitly assumes that the contact friction shear stresses reached the yield strength in shear. These results are indeed consistent with the perfectly plastic behavior after some large degree of straining. However, the independence of the straining path and isotropic behavior was not discussed in the literature. Since torsion is strongly shear-dominated, the effect of the straining path cannot be studied unless special repeated compression-torsion loadings are applied or back-and-forth torsion is used. Also, compared with force, torque gets a major contribution from the large radii, including material outside of the anvil flat faces for Brigman anvils and in the flash region for quasi-constrained HPT. In those regions, pressure is relatively low, and friction stress is determined by the Coulomb law and is smaller than the yield strength in shear. Experimental linear dependence of the steady torque versus applied pressure in Ref. [17] was related to the increase in Coulomb friction in the flash region because the effect of pressure on the yield/ultimate strength is much weaker. FEM simulations of quasi-constrained HPT of Cu in Ref. [52] utilizing Eq. (2) concluded the following. Relation between the torque and rotation angle strongly depends on the Coulomb friction coefficient μ between the flash and anvil; the best correspondence with an experiment in Ref. [53] is obtained at a relatively low $\mu = 0.12$. Therefore, stress-strain relationships obtained from torque-rotation angle functions possess significant errors. In particular, the critical plastic strain for transition to the perfectly plastic behavior, m, determined from the HPT experiments (which is in the range of $m = 5$ to 20 for Cu [17,53]), is strongly overestimated because the torque - anvil rotation angle curves are weakly dependent on the m. In particular, for uniform compression of Cu $m = 1.57$ (Table 2). Similarly, $m > 34$ for Ni [25] in HPT is an overestimation. Also, even for rough anvils surfaces, when complete adhesion is expected, analytical [54,55] and FEM [56,57] solutions predict significant relative sliding within deformed sample near the contact with anvils. The sliding was observed experimentally by disappearing the line drawn on the sample surface after some rotation, after which torque reduces [18].

Steady states after SPD in terms of grain size, dislocation density, and hardness are well-documented in literature for metals and ceramics; however, there are also reports in which they were not reached [1–7,24]. Since the yield strength can be expressed as a combination of the Taylor contribution due to dislocation density ρ and Hall-Petch contribution due to grain size d [58,59], one obtains:

$$\sigma_y = \widetilde{\sigma}_y(p) + \alpha\rho^{0.5} + \beta d^{-0.5}, \tag{3}$$

where $\widetilde{\sigma}_y(p)$ is a pressure-dependent parameter. It is clear that steady states in terms of ρ and d result in perfectly plastic pressure-dependent behavior. Since the transition to steady ρ and d are generally reached at different critical strains m, and some other parameters that possess other m (like texture) may affect σ_y, a steady state for σ_y also can be reached for different m than for microstructural parameters. We will assume in a qualitative discussion that if one of the parameters (yield strength, hardness, dislocation density, and grain size) is getting steady, then others are getting steady as well (while not all of them are reported simultaneously).

Since after HPT, uniform hardness and microstructure are reached in a major part of the sample (excluding the central region), but the shear strain is proportional to the radius, they are clearly independent of the magnitude of the plastic strain. Due to the shear-dominated character of the plastic flow during HPT, it is impossible to claim that the hardness and microstructure are independent of the straining path. In

fact, Bridgman [39] argued that reducing the strain hardening toward zero is typical for simple shear only. Segal claimed [20–22] that the straining mode (e.g., different shearing routes and the difference between simple and pure shear) affect essentially microstructure and mechanical properties; despite very large strains, a clear conclusion about perfectly plastic behavior was not made based on different straining paths during equal channel extrusion.

8. Compression and compression and shear in DAC and rotational DAC

Qualitatively new opportunities to study transition to perfect plasticity and steady microstructure emerged in experiments on compression of materials in DAC and torsion in RDAC. Due to the transparency of diamonds, pressure distributions along the radius, dislocation density, and crystallite size can be measured in situ under pressure using X-ray diffraction with synchrotron radiation and other techniques. This is much more detailed and precise information than just force, moment, hardness, and microstructural parameters measured after pressure release. It was obtained for NaCl in Ref. [60] that pressure distribution does not practically change during torsion increment in rotational DAC (RDAC) at fixed applied force after compression to a maximum pressure of 12 GPa. Corresponding analytical [54,55] and FEM [56] solutions for isotropic perfectly plastic material show the same, i.e., NaCl after plastic compression behaves like perfectly plastic and isotropic. Still, nothing can be said about strain path-independence. In Ref. [61], practically the same pressure distributions were measured after different compression-unloading-torsion programs in RDAC, ending with the same sample thickness for NaCl to a maximum pressure of 12 GPa and for hardened stainless steel to 35 GPa. These results also show the independence of the straining paths, at least for the tested paths. Note that change in the yield strength during torsion (e.g., due to phase transformation) is well visible in experiments [60,61], analytical solutions [10,11], and simulations [57,62].

Determination of linear pressure dependence of the yield strength. Finding the yield strength at high pressures is an extremely important and challenging problem because the yield strength determines the maximum static pressure that can be reached in DAC. That is why many related papers were published in highly-ranked journals [63–68]. After reaching a perfectly plastic state, the yield strength in compression σ_y or shear τ_y depends on pressure only, and this dependence was found to be linear for all studied materials [10,11,37,63–68]

$$\sigma_y = \sigma_\infty + bp; \qquad \tau_y = \sigma_y/\sqrt{3} = (\sigma_\infty + bp)/\sqrt{3}. \tag{4}$$

The pressure-dependent version of the von Mises yield condition, $\sigma_M = \sigma_\infty + bp$, was utilized. One of the methods to determine τ_y in DAC is based on applying the well-known in theory of metal forming a simplified equilibrium equation

$$\frac{d\bar{p}}{dr} = -\frac{2\tau_f}{h}, \tag{5}$$

assuming contact friction stress $\tau_f = \tau_y$ at the anvil-sample boundary (plastic friction condition) [10,11,64,65], where $\bar{p}$ is the pressure averaged over the deformed sample thickness h. With measured pressure distribution and sample thickness, two constants in the linear pressure dependence of τ_y were determined. However, since usually (excluding [10,11]) a perfectly plastic state and steady microstructure were not reached (because this was not aimed and checked and preliminary SPD was not applied), τ_y also depends on ε_p, ε_p^{path}, and grain size. This dependence was neglected, and change in τ_y was solely prescribed to change in pressure, which introduced an error. Error reduced with increasing pressure since high pressure was reached in the course of plastic compression, thus approaching a perfectly plastic state. This method was used in Refs. [10,11] to fit pressure distribution to the experimental one in Ref. [69] for a sample from T301 stainless steel compressed in DAC up to 170 GPa. The obtained result has been refined using a numerical solution with the slip lines method for a disc of perfectly plastic material compressed by rigid anvils. Despite the very small $b = 10^{-4}$, it makes visible changes in pressure distribution for such high pressure.

For ceramic and metallic anvils, pressure distribution is not available. Similar slip line solutions were used in Refs. [10,11] to fit experimental $\tilde{P}(h)$ curves to determine σ_∞ and b for pyrophyllite and two types of blocked and compacted with the Bakelite varnish and polyvinyl alcohol limestones after reaching a perfectly plastic state. A simple procedure was developed to determine σ_∞ and b separately.

In Ref. [70], the problem of compression of a rhenium sample in DAC was solved using a large-strain, isotropic, elastic-perfectly plastic model with FEM, which includes finite elastic strain in a sample and diamond and significant change in the shape of the diamond. The solution was fitted well to 3 experimental pressure distributions from Ref. [63] for pressures up to 300 GPa and reduction in thickness by a factor of 30, which allowed, in particular, to determine $\sigma_\infty = 8.00\ GPa$ and $b = 0.04$. The description of the experimental curves was much better than with the simplified model in Ref. [66]. Contact friction was described in Ref. [70] by the Coulomb friction law with a friction coefficient of 0.1, followed by $\tau_f = \tau_y(p)$ when Coloumb friction exceeded $\tau_y(p)$. However, at megabar pressure, a major part of the contact surface is under plastic friction.

A much more detailed approach was developed in Ref. [67] and applied to describe experimental results in Ref. [68] for tungsten up to 380 GPa. Four material parameters in the linear pressure dependence of the yield strength and contact stress-dependent friction coefficient have been identified to fit 2 pressure distributions up to 240 GPa. With these parameters, very good verification was shown for two other pressure distributions up to 380 GPa and four nontrivial sample thickness profiles for pressures in the range 170–380 GPa. Obtained values, $\sigma_\infty = 1.8\ GPa$ and $b = 0.1$, are much more reliable than those in the previous works [63,68], which also have very large scatter. This study also revealed various limitations. (a) The equation for σ_y is valid for $p \le 225\ GPa$ only since, for higher pressures, the sample in the central, high-pressure region deforms elastically due to cup-like deformations of the anvil-sample boundary. (b) The expression for the Coulomb friction coefficient $\mu = 0.05 + 0.001\sigma_c$, where σ_c is the normal contact stress, is valid for $\sigma_c \le 37\ GPa$ only. (c) The region with plastic friction is very small for the entire pressure range 170–380 GPa, which makes doubtful applicability of the method based on Eq. (2) for DAC because of the small friction coefficient and large deformation of diamonds and cohesion zone at high pressures.

9. In situ study of steady yield strength and microstructure in DAC with rough diamonds

Recent experiments in Ref. [71] on Zr also show that $\tau_f < \tau_y$ for pressure up to 5 GPa. To resolve the problem, diamonds with rough culets (with height of asperities of 300 nm instead of 10 nm for traditional DAC) were prepared and used to study compression of Zr up to 14 GPa in Ref. [59]. It was shown that condition $\tau_f = \tau_y$ is fulfilled at a major part of the diamond culet. This allowed us to utilize Eq. (2), or in fact, a more precise equation

$$\frac{d\bar{p}}{dr} = -\frac{2}{\sqrt{3}}\frac{1+0.524b}{1-0.262b}\frac{\sigma_\infty + b\bar{p}}{h} \tag{6}$$

to determine the pressure dependence of the yield strength. Derivation of Eq. (6) took into account the heterogeneity of all stress components along the thickness of a sample. Also, to reach a steady state, the Zr sheet was strongly predeformed by rolling from 5.25 mm to 163 μm in

7 runs (i.e., $q = 3.47$) until steady hardness was reached, thus excluding the effect of ε_p and ε_p^{path}.

After completing α→ω phase transformation, four pressure distributions have been well-described by Eq. (3) (Fig. 9) with $\sigma_\infty = 1.24\ GPa$ and $b = 0.0965 \pm 0.0016$. Also, dislocation density and crystallite size distributions, measured with in situ X-ray diffraction (XRD) under three different loads (Fig. 10), were practically independent of radius and applied load (pressure distribution). Since radial heterogeneity of ε_p, ε_p^{path}, and p is strong, and they strongly change during increasing compression, approximate independence of the microstructure of radius and compression stage implies that steady crystallite size and dislocation density are reached, which are independent of pressure, ε_p, and ε_p^{path}. Complex evolving fields of components of plastic strain tensor from FEM simulation in Ref. [72] and selected straining paths for different material points in Ref. [40] confirm essentially different ε_p, and ε_p^{path} for such a loading before, during, and after completing phase transformation.

Similar rules have been found for olivine and ringwoodite using torsion in RDAC with rough diamonds. Namely, the crystallite size and microstrain of olivine and crystallite size of

ringwoodite (during olivine-ringwoodite transformation) are getting steady and independent of ε_p, ε_p^{path}, pressure, and phase transformation progress [73]. Generally, rough diamonds essentially intensify plastic flow and also strain-induced phase transformations in DAC and RDAC [59,74,75].

10. Multiple steady states: key problems

Note that steady values of the crystallite size and dislocation density in ω-Zr are practically the same for compression with smooth and rough anvils. However, for α-Zr, three different steady states with different dislocation densities and crystallite sizes (Table 3) are obtained after multiple rolling and compression with smooth and rough diamond anvils; all are claimed to be independent of ε_p and ε_p^{path}. This is not surprising from the technological point of view since different SPD technologies lead to different steady grain sizes, dislocation densities (Fig. 11), and hardness [76,77]. However, translating these technological findings into the language of plasticity theory leads to the conclusion that there is no currently consistent theory for SPD. Indeed, a theory that includes isotropic strain path-independent limit surface of the perfect plasticity $\varphi(\boldsymbol{\sigma}) = 0$ [10,11] allows drastic simplification in the calibration of material parameters within simplified phenomenological plasticity. Suppose one knows the yield strength of an annealed material, the hardness of the material in the steady state (independent of ε_p and ε_p^{path}), and consequently, the yield strength σ_∞ (or determine pressure-dependent limit yield strength), and an estimate of strain m required for the transition to the perfectly plastic state. In that case, one can interpolate a stress-strain curve using Eq. (2), which is the main part of a 3D theory [10,11]. However, based on Fig. 11 and results with rough DAC, the steady limit σ_∞ depends on ε_p^{path} in general and in unknown ways. However, it is independent of ε_p^{path} for some paths, which were used to prove the path-independence of each limit surface of perfect plasticity. Thus, there are multiple isotropic strain path-independent limit surface of the perfect plasticity $\varphi^i(\boldsymbol{\sigma}) = 0$ (see Fig. 12 with different designations for the yield surfaces from Ref. [59]). The new key problem in the plasticity theory is: for which classes of plastic strain ε_p, strain path ε_p^{path}, pressure p, and pressure path p^{path} material deforms according to each of the surfaces $\varphi^i(\boldsymbol{\sigma}) = 0$ and for which of ε_p, ε_p^{path}, p, and p^{path} classes there are jumps from one surface to another? Pressure and pressure path are included because for plastically incompressible materials (which is a kinematic constraint on ε_p), pressure p is a reaction of the constraint and should be included along with its paths in the characterizing loading process. Note that recent in situ XRD measurements of the microstructure evolution in Zr under hydrostatic loading/unloading [78] show that the effect of pressure is hysteretic, i.e., it indeed depends on p^{path}.

This is an outstanding problem to be solved to develop a general plasticity theory for SPD, and ways to resolve it are not straightforward. Considering different straining paths in various processes in Fig. 11, we exclude ball milling from further analysis. Indeed, grain refinement in ball milling is not only due to SPD but also fracture of small particles among other processes, and also includes high strain rate heterogeneous loading and unloading, which we do not consider here. The second best grain refinement process is HPT, which distinguishes itself by higher pressure than other processes. Thus, one can hypothesize that higher pressure leads to finer microstructure, higher dislocation density, and the yield strength. However, this is not supported by experiments. According to Table 3, the pressure effect is nonmonotonous even at low pressures. Indeed, for α-Zr, dislocation density first increases, and crystallite size reduces at 0.67 GPa compared to ambient condi-

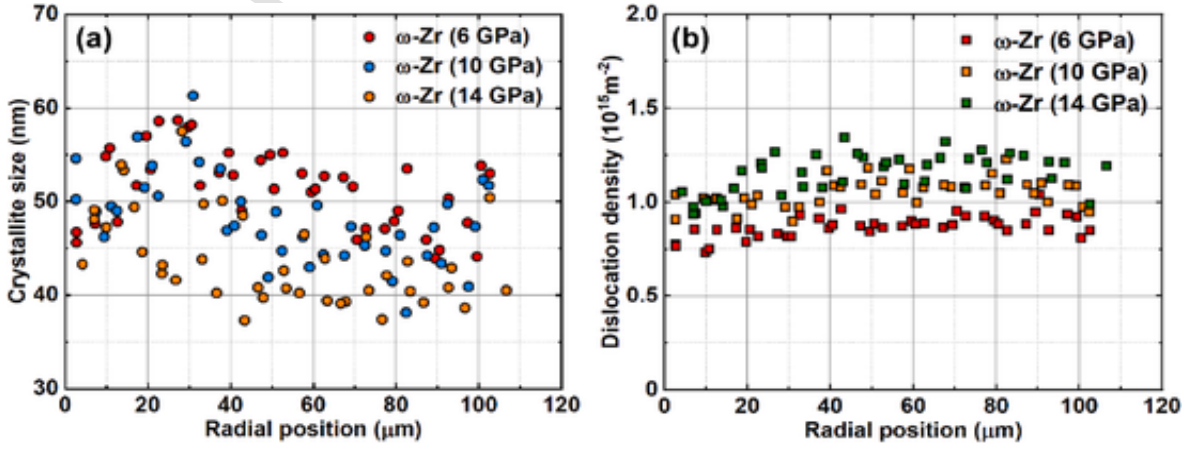

Fig. 10. Radial distribution of the crystallite size (a) and dislocation density (b) in ω-Zr for three loads. Since ε_p, ε_p^{path}, and p have significant variation along the radius and growing compression, approximate independence of the microstructure of radius and compression stage implies that steady crystallite size and dislocation density are reached, which are independent of pressure, ε_p, and ε_p^{path}. Reproduced with permission from Ref. [59].

Table 3
Crystallite size and dislocation density in α-Zr and ω-Zr for three material steady states obtained by multiple rolling and compression with smooth and rough diamond anvils (data from Ref. [59]); PT means phase transformation.

		Multiple Rolling		Smooth Anvils	Rough Anvils
Crystallite Size (nm)	α-Zr	75 ± 1 (ambient)	Steady state at PT initiation	65 ± 1 @ 1.36 GPa	48 ± 2 @ 0.67 GPa
	ω-Zr	–	Steady state after PT	49 ± 1	47 ± 6
Dislocation Density ($10^{15}m^{-2}$)	α-Zr	1.00 ± 0.02 (ambient)	Steady state at PT initiation	1.26 ± 0.07 @ 1.36 GPa	1.83 ± 0.03 @ 0.67 GPa
	ω-Zr	–	Steady state after PT	0.95 ± 0.05	1.04 ± 0.19

Table 4
Chemical composition of some alloys tested in the former USSR, for which data are presented in the current review.

Russian designation	English translation	Main elements
Ст 3 or Cm 3	St 3	Fe ~97 %; C <0.22 %, Mn < 0.65 %; Si <0.17 %; Cr <0.3 %; Cu<0.3 %; Ni <0.3 %
Сталь 10	Steel 10	Fe 97–98 %; C 0.07–0.14 %, Mn 0.35–0.65 %; Si 0.17–0.37 %; Cr <0.15 %: Cu <0.15 %; Ni <0.3 %
Сталь 20	Steel 20	Fe 97–98 %; C 0.17–0.24 %, Mn 0.35–0.65 %; Si 0.17–0.37 %; Cr <0.25 %; Cu <0.3 %; Ni <0.3 %
Сталь 45	Steel 45	Fe 97–98 %; C 0.17–0.24 %, Mn 0.5–0.8 %; Cr <0.25 %; Cu<0.3 %; Ni <0.3 %
Сталь 12ХН3А	Steel 12KhN3A	Fe >95 %; C 0.09–0.16 %, Mn 0.3–0.6 %; Cr 0.6–0.9 %: Cu<0.3 %; Ni 2.75–3.15 %
Сталь 30ХГСА	Steel 30KhGSA	Fe>95 %; C ~0.3 %, Mn 1 %; Si 1 %; Cr 1 %; Cu<0.3 %; Ni <0.3 %
Сталь 40ХНМА	Steel 40KhNMA	Fe~97 %; C 0.36–0.44 %, Mn 0.50–0.80 %; Si 0.17–0.37 %; Cr 0.80–1.10 %; Cu<0.3 %; Ni <0.3 %
Сталь У8	Steel U8	Fe>97.8 %; C 0.75–0.80 %, Mn 0.17–0.30 %; Si 0.17–0.30 %; Cr <0.20 %; Cu<0.25 %; Ni <0.25 %
Сталь У8А	Steel U8A	Fe>98 %; C 0.75–0.80 %, Mn 0.17–0.20 %; Si 0.17–0.30 %; Cr <0.20 %; Cu<0.25 %; Ni <0.25 %
Чугун В93 and В95	Cast iron V93 and V95	High strength cast iron with spherical graphite and the ultimate strength of 93 and 95 kg/mm^2 (812 and 932 MPa), respectively. Fe>90 %; C 3.2–3.6 %; Mn 0.4–0.7 %; Si 2.9–3.8 %; Cr <0.15 %; P<0.1 %; Cu <0.6 %; Ni 0.6–0.8 %
Чугун ВЧ50	Cast iron VCh50	High-strength cast iron with spherical graphite. Fe>92.4 %; C 2.7–3.7 %; Mn 0.3–0.7 %; Si 0.8–2.9 %; Cr <0.15 %; P<0.1 %
Алюминиевый сплав Д16Т	Aluminum alloy D16T	Al <94.7 %; Cu <4.9 %; Mg <1.8 %; Mn < 0.9 %; Si <0.5 %; Fe<0.5 %
алюминиевый сплав АК6	aluminum alloy AK6	Al 93.3–96.7 %; Cu 1.8–2.6 %; Mg 0.4–0.8 %; Mn 0.4–0.8 %; Si 0.7–1.2 %; Fe<0.7 %; Ni <0.1 %; Ti <0.1 %; Zn<0.3 %
Медь М2	Copper M2	Cu > 99.6 %; Ni < 0,2 %
Латунь Л62	Brass L62	Cu 61.3 %; Zn 37.9 %; Al ~0.24 %; Si ~0.19 %
Магниевый сплав Мл.5пч	Magnesium alloy Ml.5pch	Mg 89.57–92.15 %; Al 7.5–9 %; Zn 0.2–0.8 %; Mn 0.15–0.5 %

tions after rolling, but then the trend changes at 1.36 GPa. According to Fig. 10, the pressure effect on microstructural parameters in ω-Zr is within experimental error and could be due to evolving heterogeneity and texture along the sample thickness. This in situ measured pressure independence is consistent with known ex situ results after treatment at averaged pressure $\widetilde{P}$, in particular, with pressure-independence of steady hardness for single-phase Zr for $\widetilde{P} < 4$ GPa and $6 < \widetilde{P} < 40$ GPa [79], Ni for $3 < \widetilde{P} < 9$ GPa [2,80], Fe for $\widetilde{P} < 7$ GPa and $28 < \widetilde{P} < 40$ GPa [24], and Ti for $\widetilde{P} < 4$ GPa and $20 < \widetilde{P} < 40$ GPa [81]. Pressure-independent grain sizes have been demonstrated in V [82], Au, Ag, Hf, Cu, Pt, Al, and Cu–30 %Zn [24]. Some numerical estimates for justification of the pressure-independence of the grain size for ω-Zr are presented in Ref. [59]. They are based on the analysis of pressure dependence of the main parameters that participate in some empirical relationships for steady grain size, like the magnitude of Burgers vector, self-diffusion activation energy, and the frequency factor for pipe diffusion, shear modulus, stacking fault energy, hardness, melting temperature, etc. [83,84]. Still, different pressure paths along with ε_p and ε_p^{path} could affect the steady yield strength and microstructure.

The following approaches could be outlined to resolve this problem. In FEM simulations of each of the technological processes, loading paths at each material integration point should be determined (e.g., like in Ref. [40]), analyzed, and classified according to determined criteria, including loading mode, monotonicity (unloading and reloading, sharp changes, etc.), curvature of the straining and pressure trajectory, produced texture, and geometry and orientation of grains. Obtained averaged characteristics of the loading paths should be connected to the steady grain size, dislocation density, and yield strength, possibly utilizing machine learning techniques.

Note that small strain Il'yushin's theory of plasticity [85–87] is based on the classification of loading processes in 5D deviatoric strain and stress spaces based on the curvature, like simple loading along a straight line, small, middle, and arbitrary curvature processes, two and multilink trajectories with corners (which include elastic unloading), etc., without referring to microstructure. Generalization of Il'yushin's theory for the large strain was suggested in Refs. [10,11] utilizing path-dependent strain measure ε_p^L, which is a deviatoric tensor for plastically incompressible materials and is work-conjugate with the deviatoric true (Cauchy) stress $\boldsymbol{s}$. If the strain path is characterized in terms of $\varepsilon_p^{L,path}$ prior to the current state ε_p^L, the isotropic limit surface of perfect plasticity can be presented as $\varphi^i\left(\sigma, p^{path}, J_2^L, J_3^L\right) = 0$, where J_i^L is the ith invariant of $\varepsilon_p^{L,path}$, since $J_1^L = 0$.

Fixed limit surfaces of perfect plasticity can also be obtained from crystal plasticity simulations for different crystal symmetries and loading paths, providing that the physics of single crystal plasticity and interaction between crystals is described with proper accuracy. However, at the initial stage, even utilizing the simplest single crystal plasticity theory and Taylor equal strain assumptions may guide which parameters are responsible for jumping from one limit surface of perfect plasticity to another.

Mathematically, the evolution equation for dislocation density and grain size has the following structure

$$\frac{da}{dq} = A^+ - A^-, \tag{7}$$

where A^+ and A^- are positive and negative contributions to the growth of a. For example, for dislocation density, A^+ is due to dislocation multiplication, and A^- is due to their annihilation; for grain size, A^- is due to traditional mechanisms of grain refinement, and A^+ is due to dynamic recrystallization and grain boundary migration. Steady state corresponds to $A^+ = A^-$ independent of the initial conditions. This corresponds to experiments on HPT of Ni [3,26,88], steel [89], and copper [90]: if the initial grain size is smaller than the steady one, SPD leads to grain growth to the same steady state as when starting with coarse-grained material. Thus, making coefficients in A^+ and A^- dependent on some characteristics of ε_p^{path} and p^{path} solves the problem of obtaining different steady states. However, it is unclear how to get the same steady state for a broad class of ε_p^{path} and p^{path} and jump to other steady

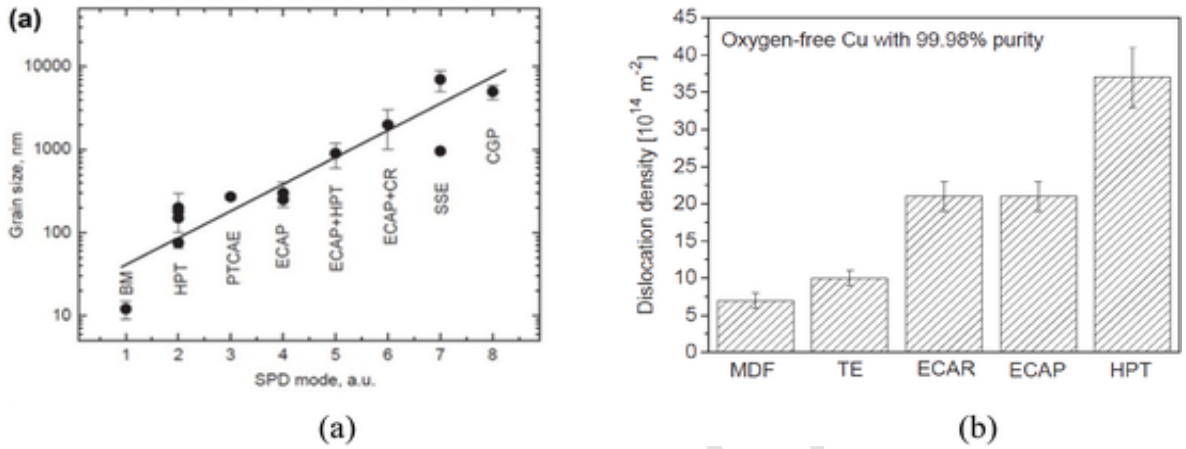

Fig. 11. Steady-state grain size and dislocation density in Cu subjected to different SPD modes collected from various sources. (a) 1- ball milling (BM), 2- HPT, 3- planar twist channel angular extrusion (PTCAE), 4- equal-channel angular pressing (ECAP), 5- ECAP + HPT, 6- ECAP with following cold rolling (ECAP + CR), 7- simple shear extrusion (SSE), and 8- constrained groove pressing. Reproduced with permission from Ref. [76]. (b) Multi-directional forging (MDF), twist extrusion (TE), and equal channel angular rolling (ECAR). Reproduced with permission from Ref. [77].

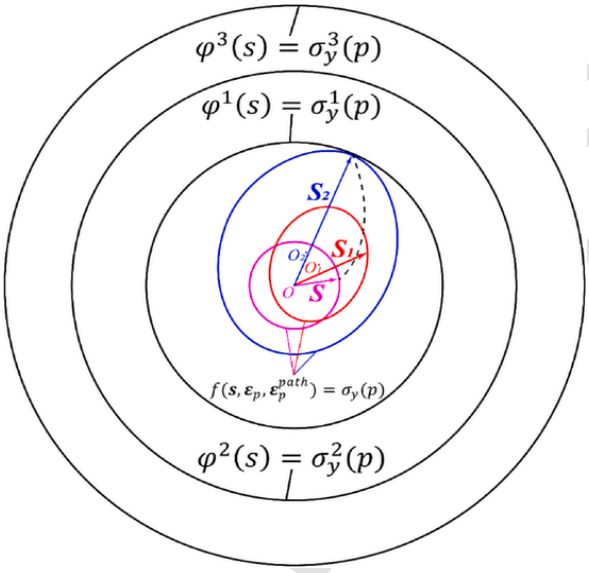

Fig. 12. Sketch of the evolution of the yield surface $f\left(s, \varepsilon_p, \varepsilon_p^{path}\right) = \sigma_y(p)$ in 5D space of deviatoric stresses s at fixed p until it reaches the fixed isotropic limit surface of perfect plasticity $\varphi(s) = \sigma_y^1(p)$, after which the material deforms like perfectly plastic, isotropic with the fixed limit surface of perfect plasticity. However, for some classes of plastic strain paths ε_p^{path}, multiple other fixed limit surfaces of perfect plasticity $\varphi^i(s) = \sigma_y^i(p)$ with different yield strengths $\sigma_y^i(p)$ can be accessed. Reproduced with permission from Ref. [59].

states for other broad classes of ε_p^{path} and p^{path}, and how to classify and separate these classes.

Note that the dependence of the isotropic limit surface of perfect plasticity on ε_p^{path} does not mean that the theory of SPD, even for the steady state, possesses similar complexity to the theory before reaching the steady state, i.e., that the existence of the steady state does not simplify theory. Indeed, for each of the technological processes in Fig. 11 and experiments leading to the conclusion of the independence of the limit surface of perfect plasticity on ε_p^{path}, quite broad classes of ε_p^{path} have been utilized, while not completely classified. This means that for these experiments and processes, theory with the single surface $\varphi(\boldsymbol{\sigma}) = 0$ with a steady yield strength (pressure dependent or not) determined for this process through hardness measurement or utilizing the experiment in DAC described above is applicable. Indeed, defined in such a way, the simple isotropic limit surface of perfect plasticity $\varphi(\boldsymbol{\sigma}) = 0$ reproduced the complex experimental distribution of the evolution of the distribution of multiple measured parameters (pressure, radial and hoop elastic strains, and complex shape of the sample) [59,67,70,72].

The independence of the final microstructure and properties of the initial one is a part of the strain-path independence of the surface of perfect plasticity if different initial microstructures are obtained by different plastic straining. However, different initial microstructures can be caused by different preparation methods, e.g., by pressing/sintering powders with different grain sizes.

11. Ultra-small strain hardening during ultra-SPD

Different studies indicate different values m for reaching steady yield strength and microstructures. While uniform compression and Bridgman anvil experiments [10,11,15,36–38] give $0.4 < m < 1.6$ with smaller values for minerals and higher for metals, HPT experiments suggest large scatter even for the same material (e.g., $m = 5$ to 20 for Cu [17,53]) and even larger values $m > 34$ for Ni [3,25] with HPT. Parameter m can of course, depend on the straining mode, but hardly to such an extent; other reasons related to HPT are discussed above.

Work [31] pioneered research on ultra-SPD with shear strain $\gamma > 1000$, and reported that after a plateau in hardness, a new hardening stage after HPT starts at $\gamma > 800 - 2,000$ for Ti, Ni, and Fe. A more focused study [23] found that despite a large scatter, a hardening rate of 0.42 MPa for Fe and 0.22 MPa for Ni can be deduced for $q < 275$, i.e., below the ultra – SPD regime. The scatter in data was up ~200 MPa for Fe and up to ~100 MPa for Ni, equivalent for such a hardening rate to $q \cong 465$. For the range $10^3 < q < 8.5 \times 10^4$, hardening with a very small rate of 0.03 MPa is reported after some steady state. Various hypothetical reasons for the reappearing of the hardening are discussed in Refs. [23,29,31], including surface alloying, increased density of point defects, transition in controlling deformation mechanisms, and transition from laminar to turbulent flow. Without discussing these reasons, we would like to add one more related to the

change in microstructure during unloading after HPT and the difference between in-situ and ex-situ studies.

(a) While for practical applications properties of the sample after SPD and pressure release are significant, plasticity theory describes processes during HPT or other high-pressure SPD. With a generic pressure hardening parameter in Eq. (4) $b \cong 0.1$ and an averaged pressure of 7.8 or 4 GPa used in Ref. [23], the pressure-induced change in the yield strength is 780 or 400 MPa, which translates into a change in hardness of 2.34 or 1.20 GPa. Thus, a small change in hardness (i.e., in σ_∞) with strain can be compensated by a small change in b with strain, resulting in a negligible strain effect on the pressure-dependent yield strength.

(b) During unloading after HPT of Ni, crystallite size grows, and dislocation density reduces by a factor of 2 [91]. For comparison, increment in q from 50 to 250 for Ni reduces grain size from 250 nm to 200 nm [23]. This difference could be not because of a grain size reduction during plastic flow under pressure but due to a change in grain size growth during unloading. Also, pressure distribution during HPT is heterogeneous [52,53], but most important, it can reduce during rotations due to plastic deformation of anvils, reduction in sample thickness, and also after switching from anvils with larger to smaller depths. Smaller pressure in the experiment can lead to smaller grain growth during unloading and reduced with straining measured grain size after pressure release. That is why in situ *measurements* of the microstructural parameters and pressure-dependent yield strength in DAC and RDAC are of great importance for correct conclusions. Also, using diamond anvils with rough diamonds [59,74,75] eliminates the potential effect of mechanical alloying from the metallic/ceramic anvils. Note that a significant variation of dislocation density and crystallite size was observed in situ under hydrostatic loading of Zr [78].

Finally, even if strain hardening with the reported small rate occurs in situ, it is relevant for ultra-SPD only and is undetectable at smaller strains. Also, any statement about the independence of one parameter from another is true within some range of change of the governing parameters, accuracy of the measurement and scatter, and acceptable error. With increased accuracy and range of change of the governing parameter, small variations can be taken into account, which does not reduce the importance of the statement about independence and corresponding models. Since no results related to strain path dependence and anisotropy have been found so far, including weak dependence of the surface $\varphi(\boldsymbol{\sigma}) = 0$ on q is sufficient.

12. Concluding remarks

The main fundamental challenge in studying plastic flow and microstructure evolution is that these processes depend not only on the current plastic strain tensor ε_p (already challenging enough) but also on its whole straining path ε_p^{path} prior to ε_p. Since for plastically incompressible material, five components of the plastic strain tensor are independent only, and one also has to include pressure p (as a reaction of the constraint) and its path p^{path} in the list of independent parameters. Due to the infinite number of independent parameters, this makes finding some general rules close to impossible.

In the review, we collected and analyzed experimental results confirming the validity of the following hypothesis formulated in Refs. [10,11] and its possible generalization: after some critical level of SPD and monotonic and quasi-monotonic straining paths, initially isotropic polycrystalline materials behave like perfectly plastic, isotropic, and strain-path-independent with the corresponding limit surface of perfect plasticity, and reach steady values of the crystallite/grain size and dislocation density, which are strain- and strain-path-independent. These rules drastically simplify the general 3D theory of SPD, the development of specific models, and the experimental determination of material functions and parameters. Relatively simple determination of the parameters of the isotropic limit surface of perfect plasticity allows us to find approximate models for materials behavior in the entire strain range by interpolation.

For non-monotonic loading, materials behave according to their actual yield surface $f\left(\boldsymbol{\sigma}, \varepsilon_p, \varepsilon_p^{path}\right) = 0$, i.e., like anisotropic and dependent on plastic strain and its path. However, for non-monotonic straining started from the surface $\varphi(\boldsymbol{\sigma}) = 0$, after further monotonic straining with increments exceeding some relatively small critical value $q^* \cong 0.1$ (quasi-monotonic loading), the stress vector and yield surface $f\left(\boldsymbol{\sigma}, \varepsilon_p, \varepsilon_p^{path}\right) = 0$ touch again the same limit surface of the perfect plasticity $\varphi(\boldsymbol{\sigma}) = 0$, and the material again behaves like perfectly plastic, isotropic, and strain path independent.

The key problem is that the experiments exhibit multiple steady microstructural states and corresponding limit surfaces of perfect plasticity, obtained by different SPD techniques or by smooth or rough diamond anvils. The main challenge is to find for which classes of loading paths ε_p^{path} and p^{path} material behaves along the same limit surface of perfect plasticity and steady microstructural states and for which loading paths ε_p^{path} and p^{path} there is a jump to the different limit surface of perfect plasticity and steady microstructural state. This is an open problem, and without its solution, the general theory of SPD does not exist. However, for the similar classes of the loading paths ε_p^{path} and p^{path} (while not well defined) for the chosen SPD technology or loading process, one can use theory plasticity with the corresponding fixed limit isotropic surfaces of perfect plasticity and steady values of the crystallite/grain size and dislocation density corresponding to this technology. As an example, determined in such a way, the simple isotropic limit surface of perfect plasticity expressed in terms of the equivalent von Mises stress and linear pressure dependence of the yield strength reproduced complex experimental evolution of the distribution of various measured parameters (pressure, radial and hoop elastic strains, and complex shape of the sample) [59,67,70,72].

Various methods have been used to prove the validity or plausibility of the above hypotheses, partially or in whole. They include severe quasi-homogeneous and homogeneous deformations of a sample, which allow, in particular, to determine the equivalent strain m necessary for reaching the steady state and corresponding equivalent stress σ_∞. Based on literature data, m for the same material varies in a very broad range depending on the testing method (i.e., straining mode and path), and in many experiments perfectly plastic state was not reached. The main problem is to find how m and σ_∞ depend on the straining mode and path. While experiments with heterogeneous fields, particularly in various SPD technologies, provide broad classes of straining modes and paths, extracting data from them is challenging and often misleading. New opportunities emerged under high pressure utilizing in situ XRD measurements of the radial distributions of pressure or elastic radial and hoop strains, dislocation density, and crystallite size in DAC and RDAC, especially in combination with FEM simulations and extraction of the pressure-dependent yield strength [59,63,67,68,70,73]. Since a broad spectrum of the straining and pressure paths are involved in these experiments, independence of the measured parameters of the straining and pressure paths can be concluded from those experiments.

Some intriguing results require their explanation. They include (a) much higher yield strength after multiple drawings than for other deformation modes [13,29]; (b) the same steady hardness after multiple broaching and in the neck of the fractured specimen or broken cross-section of compressed to fracture specimen [41] and after compression of the apex of a conical sample along its axis [49], i.e., at very different straining paths, and (c) different steady states obtained by increasing

contact friction during compression in DAC [59], i.e., at quite close straining paths.

Ultra-small strain hardening at ultra-SPD revealed in Refs. [23,31] (even if confirmed that this is not an artifact of mechanical alloying) does not spoil the above hypotheses and rules about steady states and perfectly plastic behavior. Any statement about the independence of one parameter of another is true within some range of change of the governing parameters, accuracy of the measurement and scatter, and acceptable error. Observed ultra-small strain hardening is relevant for ultra-SPD only and is undetectable for smaller strain ranges of major interest. With increased accuracy and range of change of the governing parameter, slight variations can be taken into account, which does not reduce the importance of the statement about independence and corresponding models. Since no results related to strain path dependence and anisotropy have been found so far, including weak dependence of the surface $\varphi(\sigma) = 0$ on q is sufficient.

Note that there are other steady states after SDP not covered in the current review. In particular, after reaching steady yield strength, dislocation density, and crystallite size, the minimum pressure for plastic strain-induced phase transformations is also getting steady and independent of the plastic strain tensor and its path [71–73,75,92,93]. Also, SPD-induced composition and, in some cases, the volume fraction of a high-pressure phase reach a steady state, independent of the initial state [76,94]. Independence of the steady volume fraction of a high-pressure phase was predicted analytically [54,55] for the case when direct and reverse strain-induced transformation can occur simultaneously. Steady stresses and microstructural parameters related to the high-temperature creep and cyclic deformations are analyzed in Ref. [95]. The perfectly plastic model is broadly used for studying phase transformations in plastic materials [96]. Various aspects of the effect of SPD have been reviewed in the recent comprehensive papers [97,98].

Data availability

Data will be made available on request.

Declaration of competing interest

The authors declare the following financial interests/personal relationships which may be considered as potential competing interests: Valery I. Levitas reports financial support was provided by US National Science Foundation and US Army Research Office. If there are other authors, they declare that they have no known competing financial interests or personal relationships that could have appeared to influence the work reported in this paper.

Acknowledgments

The author acknowledges the support of the US National Science Foundation (DMR-2246991), the US Army Research Office (W911NF2420145) and Iowa State University (Vance Coffman Faculty Chair Professorship and Murray Harpole Chair in Engineering). The simulations were performed at Extreme Science and Engineering Discovery Environment (XSEDE), allocation TG-MSS170015. The author greatly appreciates and enjoyed collaboration with all his coauthors of papers cited here, including graduate students, postdocs, and faculty and researchers from different organizations.

Appendix A. Supplementary data

Supplementary data to this article can be found online at https://doi.org/10.1016/j.jmrt.2025.03.060.

References

[1] Edalati K, Bachmaier A, Beloshenko V.A, et al. Nanomaterials by severe plastic deformation: review of historical developments and recent advances. Mater Res Lett 2022;10(4):163–256.
[2] Zhilyaev A.P, Langdon T.G. Using high-pressure torsion for metal processing: fundamentals and applications. Prog Mater Sci 2008;53:893–979.
[3] Pippan R, Scheriau S, Taylor A, et al. Saturation of fragmentation during severe plastic deformation. Annu Rev Mater Res 2010;40:319–43.
[4] Cao Y, Ni S, Liao X, Song M, Zhu Y. Structural evolutions of metallic materials processed by severe plastic deformation. Mater Sci Eng R Rep 2018;133:1–59.
[5] Valiev R.Z, Estrin Y, Horita Z, Langdon T.G, Zechetbauer M.J, Zhu Y.T. Producing bulk ultrafine-grained materials by severe plastic deformation. JOM 2006;58:33–9.
[6] Valiev R.Z, Estrin Y, Horita Z, Langdon T.G, Zechetbauer M.J, Zhu Y.T. Producing bulk ultrafine-grained materials by severe plastic deformation: ten years later. JOM 2016;68:1216–26.
[7] Zhu Y.T, Langdon T.G. The fundamentals of nanostructured materials processed by severe plastic deformation. JOM 2004;56(10):58–63.
[8] Girard J, Amulele G, Farla R, Mohiuddin A, Karato S. Shear deformation of bridgmanite and magnesiowüstite aggregates at lower mantle conditions. Science 2016;351(6269):144–7.
[9] Levitas V.I. Resolving puzzles of the phase-transformation-based mechanism of the strong deep-focus earthquake. Nat Commun 2022;13(1):6291.
[10] Levitas V.I. Large elastoplastic deformations of materials at high pressure. Kiev: Naukova Dumka; 1987.
[11] Levitas V.I. Large deformation of materials with complex rheological properties at normal and high pressure. New York: Nova Science; 1996.
[12] Lubarda V. Elastoplasticity theory. Boca Raton: CRC Press; 2001.
[13] Sevillano J.G, Houtte P.V, Aernoudt E. Large strain work hardening and textures. Prog Mater Sci 1980;25:69–134.
[14] Brown S.B, Kim K.H, Anand L. An internal variable constitutive model for hot working of metals. Int J Plast 1989;5:95–130.
[15] Levitas V.I, Stashkevich I.E, Nemirovskii A.B. Stress-strain diagrams of metals under large uniform compressive strains. Strength Mater 1994;26:676–80.
[16] Pippan R, Wetscher F, Hafok M, Vorhauer A, Sabirov I. The limits of refinement by severe plastic deformation. Adv Eng Mater 2006;8:10461056.
[17] Hafok M, Pippan M. Influence of stacking fault energy and alloying on stage V hardening of HPT-deformed materials. Int J Mat Res 2010;101:1097–104.
[18] Hohenwarter A, Bachmaier A, Gludovatz B, Stephan S, Pippan R. Technical parameters affecting grain refinement by high pressure torsion. Int J Mater Res 2009;100:1653–61.
[19] Segal V.M, Reznikov V.I, Drobyshevkij A.E, Kopylov V.I. Plastic treatment of metals by plastic shear. Russ Metall 1981;1:115–23.
[20] Segal V.M. Materials processing by simple shear. Material Science and Engineering A 1995;1971:57–164.
[21] Segal V.M. Severe plastic deformation: simple shear versus pure shear. Material Science and Engineering A 2002;338:331–44.
[22] Segal V.M. Review: modes and processes of severe plastic deformation (SPD). Materials 2018;11:1175.
[23] Renk O, Hohenwarter A, Edalati K, Marlene W.K. Saturation of grain fragmentation upon severe plastic deformation: fact or fiction? Adv Eng Mater 2024;2400578.
[24] Edalati K, Horita Z. Universal plot for hardness variation in pure metals processed by high-pressure torsion. Mater Trans 2010;51:1051–4.
[25] Zhang H.W, Huang X, Hansen N. Evolution of microstructural parameters and flow stresses toward limits in nickel deformed to ultra-high strains. Acta Mater 2008;56:5451–65.
[26] Yang B, Vehoff H, Hohenwarter A, Hafok M, Pippan R. Strain effects on the coarsening and softening of electrodeposited nanocrystalline Ni subjected to high pressure torsion. Scr Mater 2008;58:790–3.
[27] Rollett A.D, Kocks U.F. A review of the stages of work hardening. Solid State Phenom 1993;35–36:1–18.
[28] Kocks U.F, Mecking H. Physics and phenomenology of strain hardening: the FCC case. Prog Mater Sci 2003;48:171273.
[29] Sevillano J.G. Dynamic steady state by unlimited unidirectional plastic deformation of crystalline materials deforming by dislocation glide at low to moderate temperatures. Metals 2020;10:66.
[30] Kocks U.F, Tomé C.N, Wenk H.R. Texture and anisotropy. Preferred orientations in polycrystals and their effect on material properties. Cambridge: Cambridge University Press; 2000.
[31] Edalati K. Metallurgical alchemy by ultra-severe plastic deformation via high-pressure torsion process. Mater Trans 2019;60:12211229.
[32] Edalati K. Superfunctional materials by ultra-severe plastic deformation. Materials 2023;16:587.
[33] Hill R. Mathematical theory of plasticity. Oxford: Oxford University Press; 1950.
[34] Giginjak F.F, Lamashevsky V.P, Koval'chuk B.I, Lebedev A.A. Handbook of mechanical properties of structural materials at a complex stress state. Begell House; 2001.
[35] Khan A.S, Huang S. Continuum theory of plasticity. New York, Toronto: John Wiley & Sons; 1995.
[36] Wakatsuki M, Ichirlose K, Aoki T. Notes on compressible gasket and Bridgman anvil-type high pressure apparatus. Jap J Appl Phys 1972;11:578–96.
[37] Bakul V.N, Gerasimovich A.V, Ivakhnenko S.A. Pressure Dependence of shear strength of lithographic limestone and pyrophyllite. Synthetic Diamonds 1976;2:

25–30.
[38] Gerasimovich A.V, Kulemza V.A, Krikun V.I. Examination of materials of high pressure apparatus deformable gasket. Superhard Materials 1982;4:9–11.
[39] Bridgman P.W. Studies in large plastic flow and fracture with special emphasis on the effects of hydrostatic pressure. New York-Toronto-London: McGraw-Hill; 1952.
[40] Dhar A, Levitas V.I, Pandey K.K, Park C, Somayazulu M, Velisavljevic N. Quantitative kinetic rules for plastic strain-induced α-ω phase transformation in Zr under high pressure. npj Comput Mater 2024;10:290 (unpublished data).
[41] Rosenberg O.A. Mechanics of interaction of tool with product at deforming broaching. Kiev: Naukova Dumka; 1981.
[42] Grozinskaya Z.P. Surface hardening of metals by rolling, surface quality of machine parts. Moscow, the USSR Academy of Sciences 1959;4:158–63.
[43] Rosenberg A.M, Rosenberg O.A, Posvyatenko E.K, et al. Calculation and design of cemented carbide deforming broach and process of broaching. Kiev: Naukova Dumka; 1978.
[44] Del G.D. Determination of stress in plastic region on hardness distribution. 1971. Moscow, Mashinostroenie.
[45] lshlinsky A.Y. Axisymmetrical problem of plasticity theory and Brinel test. Appl Math Mech 1944;8:201–28.
[46] Del' GD. Technological mechanics. 1978. Moscow, Mashinostroenie.
[47] Pavlina E.J, Tyne C.J.V. Correlation of yield strength and tensile strength with hardness for steels. J Mater Eng Perform 2008;17:888–93.
[48] Zhang P, Li S.X, Zhang Z.F. General relationship between strength and hardness. Mater Sci Eng 2011;529:62–73.
[49] Rozenberg AM, Levitas VI, Rozenberg OA, Nemirovskiy YB, Krivosheya VV, Chernyavskiy AV, et al. Method of materials limit hardness determination. Invention certificate No. 1422108.
[50] Voce E. The relationship between stress and strain for homogeneous deformations. J Inst Metals 1948;74:537–62.
[51] Voce E. A practical strain hardening function. Metallurgia 1955;51:219–26.
[52] Kamrani M, Levitas V.I, Feng B. FEM simulation of large deformation of copper in the quasi-constrained high-pressure-torsion setup. Mater Sci Eng 2017;705:219–30.
[53] Edalati K, Lee D.J, Nagaoka T, Arita M, Kim H.S, Horita Z, Pippan R. Real hydrostatic pressure in high-pressure torsion measured by bismuth phase transformations and fem simulations. Mater Trans 2016;57:533–8.
[54] Levitas V.I. High pressure mechanochemistry: conceptual multiscale theory and interpretation of experiments. Phys Review B 2004;70:184118.
[55] Levitas V.I. Continuum mechanical fundamentals of mechanochemistry. In: Gogotsi Y, Domnich V, editors. High pressure surface science and engineering, section 3. Bristol and Philadelphia: Institute of Physics; 2004. p. 159–292.
[56] Levitas V.I, Zarechnyy O.M. Numerical study of stress and plastic strain evolution under compression and shear of a sample in rotational anvil cell. High Press Res 2010;30:653669.
[57] Levitas V.I, Zarechnyy O. Modeling and simulation of strain-induced phase transformations under compression and torsion in a rotational diamond anvil cell. Phys Rev B 2010;82:174124.
[58] Voyiadjis G.Z, Yaghoobi M. Size effects in plasticity: from macro to nano. Cambridge: Academic Press; 2019.
[59] Lin F, Levitas V.I, Pandey K.K, Yesudhas S, Park C. In-situ study of rules of nanostructure evolution, severe plastic deformations, and friction under high pressure. Materials Research Letters 2023;11(9):757–63.
[60] Blank V.D, Estrin E.I. Phase transitions in solids under high pressure. CRC Press; 2013.
[61] Novikov N.V, Polotnyak S.B, Shvedov L.K, Levitas V.I. Regularities of phase transformations and plastic straining of materials in compression and shear on diamond anvils: experiments and theory. J Superhard Mater 1999;21:36–48.
[62] Feng B, Levitas V.I, Kamrani M. Coupled strain-induced alpha to omega phase transformation and plastic flow in zirconium under high pressure torsion in a rotational diamond anvil cell. Mater Sci Eng 2018;731:623–33.
[63] Hemley R.J, Mao H.K, Shen G.Y, Badro J, Gillet P, Hanfland M, Hausermann D. X-Ray imaging of stress and strain of diamond, iron, and tungsten at megabar pressures. Science 1997;276:1242–5.
[64] Meade C, Jeanloz R. The strength of mantle silicates at high pressures and room temperature: implications for the viscosity of the mantle. Nature 1990;348:533–5.
[65] Meade C, Jeanloz R. Effect of a coordination change on the strength of amorphous SiO2. Science 1988;241(4869):1072–4.
[66] Merkel S, Hemley R.J, Mao H.K. Finite-element modeling of diamond deformation at multimegabar pressures. Appl Phys Lett 1999;74:656–8.
[67] Levitas V.I, Kamrani M, Feng B. Tensorial stress-strain fields and large elastoplasticity as well as friction in diamond anvil cell up to 400 GPa. npj Comput Mater 2019;5(1):94.
[68] Bing L, Cheng J, Wenge Y, Junyue W, Ke Y, Ruqing X, Wenjun L, Zhonghou C, Jiuhua C, Mao H.K. Diamond anvil cell behavior up to 4 mbar. Proc Natl Acad Sci USA 2018;115:1713–7.
[69] Mao H.K, Bell P.M. High-pressure physics: the 1-megabar mark on the ruby R1 static pressure scale. Science 1976;191:851–2.
[70] Feng B, Levitas V.I, Hemley R.J. Large elastoplasticity under static megabar pressures: formulation and application to compression of samples in diamond anvil cells. Int J Plasticity 2016;84:33–57.
[71] Pandey K.K, Levitas V.I. In situ quantitative study of plastic strain-induced phase transformations under high pressure: example for ultra-pure Zr. Acta Mater 2020;196:338–46.
[72] Levitas V.I, Dhar A, Pandey K.K. Tensorial stress-plastic strain fields in α-ω Zr mixture, transformation kinetics, and friction in diamond anvil cell. Nat Commun 2023;14:5955.
[73] Lin F, Levitas V.I, Yesudhas S, Smith J. Severe strain-induced olivine-ringwoodite transformation at room temperature: key to enigmas of deep-focus earthquake. SSRN July 05, 2024:29 https://doi.org/10.2139/ssrn.4893171. (unpublished data).
[74] Lin F, Levitas V.I, Pandey K.K, Yesudhas S, Park C. Laws of high-pressure phase and nanostructure evolution and severe plastic flow. Research Square 2022:29 https://doi.org/10.21203/rs.3.rs-1998605/v1. (unpublished data).
[75] Yesudhas S, Levitas V.I, Lin F, Pandey K.K, Smith J. Unusual plastic strain-induced phase transformation phenomena in silicon. Nat Commun 2024;15:7054.
[76] Mazilkin A, Straumal B, Kilmametov A, Straumal P, Baretzky B. Phase transformations induced by severe plastic deformation. Mater Trans 2019;60:1489–99.
[77] Gubicza J. Lattice defects and their influence on the mechanical properties of bulk materials processed by severe plastic deformation. Mater Trans 2019;60:1230–42.
[78] Pandey K.K, Levitas V.I, Park C. In situ study of microstructure evolution and α→ω phase transition in annealed and pre-deformed Zr under hydrostatic loading. J Appl Phys 2024;136:115901.
[79] Edalati K, Horita Z, Yagi S, Matsubara E. Allotropic phase transformation of pure zirconium by high-pressure torsion. Mater Sci Eng A 2009;523:277–81.
[80] Zhilyaev A.P, Nurislamova G.V, Kim B.K, Baro M.D. Experimental parameters influencing grain refinement and microstructural evolution during high-pressure torsion. Acta Mater 2003;51:753–65.
[81] Edalati K, Matsubara E, Horita Z. Processing pure Ti by high-pressure torsion in wide ranges of pressures and strain. Metall Mater Trans A 2009;40:2079–86.
[82] Lee S, Edalati K, Horita Z. Microstructures and mechanical properties of pure V and Mo processed by high-pressure torsion. Mater Trans 2010;51:1072–9.
[83] Mohamed F.A. A dislocation model for the minimum grain size obtainable by milling. Acta Mater 2003;51(14):4107–19.
[84] Mohamed F.A, Dheda S.S. On the minimum grain size obtainable by high-pressure torsion. Mater Sci Eng A 2012;558:59–63.
[85] Il'yushin A.A. Plasticity. Moscow: Publisher of Academy of Sciences of USSR; 1963.
[86] Il'yushin A.A. Continuum mechanics. Moscow: Moscow University; 1978.
[87] Lenskii V.S. Experimental corroboration of basic postulates of a general theory of elastic-plastic strains. In: Problems of the theory of plasticity; 1961. p. 58–82. Moscow.
[88] Liao X.Z, Kilmametov A.R, Valiev R.Z, Gao H, Li X, Mukherjee A.K, Bingert J.F, Zhu Y.T. High-pressure torsion-induced grain growth in electrodeposited nanocrystalline Ni. Appl Phys Lett 2006;88:021909.
[89] Borchers C, Garve C, Tiegel M, Deutges M, Herz A, Edalati K, Pippan R, Horita Z, Kirchheim R. Nanocrystalline steel obtained by mechanical alloying of iron and graphite subsequently compacted by high-pressure torsion. Acta Mater 2015;97:207–15.
[90] Wen H, Islamgaliev R.K, Nesterov K.M, Valiev R.Z, Lavernia E.J. Dynamic balance between grain refinement and grain growth during high-pressure torsion of Cu powders. Philos Mag Lett 2013;93:481–9.
[91] Kerber M.B, Spieckermann F, Schuster R, Baeckmann C, Fischer T, Schell N, et al. In situ synchrotron X-ray diffraction during high-pressure torsion deformation of Ni and NiTi. Adv Eng Mater 2021;23:2100159.
[92] Levitas V.I. High-pressure phase transformations under severe plastic deformation by torsion in rotational anvils. Material Transactions 2019;60:1294–301.
[93] Levitas V.I. Recent in situ experimental and theoretical advances in severe plastic deformations, strain-induced phase transformations, and microstructure evolution under high pressure. Material Transactions 2023;64:1866–78.
[94] Straumal B.B, Kilmametov A.R, Ivanisenko Y, Mazilkin A.A, Kogtenkova O.A, Kurmanaeva L, Korneva A, Zięba P, Baretzky B. Phase transitions induced by severe plastic deformation: steady-state and equifinality. Int J Mater Res 2015;106:657–64.
[95] Mughrabi H. Revisiting ''Steady-State'' monotonic and cyclic deformation: emphasizing the quasi-stationary state of deformation. Metall Mater Trans 2020;51A:1441–56.
[96] Levitas V.I. Phase transformations, fracture, and other structural changes in inelastic materials. Int J Plast 2021;140:102914.
[97] Edalati K, Bachmaier A, Beloshenko V.A, et al. Nanomaterials by severe plastic deformation: review of historical developments and recent advances. Mater Res Lett 2022;10:163–256.
[98] Edalati K, Ahmed A.Q, Akrami S, et al. Severe plastic deformation for producing superfunctional ultrafine-grained and heterostructured materials: an interdisciplinary review. J Alloys Comp 2024;2002:174667.